Precambrian faulting episodes and insights into the tectonothermal history of North Australia: Microstructural evidence and K–Ar, ^{40}Ar–^{39}Ar, and Rb–Sr dating of syntectonic illite from the intracratonic Millungera Basin.

I. Tonguç Uysal[1], Claudio Delle Piane[2], Andrew Todd[2] and Horst Zwingmann[3]

[1]Ankara University, Geological Engineering Department, Gölbaşı, Ankara, Turkey

[2]CSIRO Energy, 26 Dick Perry Avenue, Kensington WA 6151, Australia

[3]Department of Geology and Mineralogy, Kyoto University, Kitashirakawa Oiwake-cho, Kyoto 606-8502, Japan.

ABSTRACT

Australian terranes concealed beneath Mesozoic cover record complex Precambrian tectonic histories involving a successive development of several Proterozoic to Paleozoic orogenic systems. This study presents an integrated approach combining K–Ar, ^{40}Ar–^{39}Ar, and Rb–Sr geochronology of Precambrian authigenic illites from the recently discovered Millungera Basin in north-central Australia. Brittle deformation and repeated fault activity are evident from the sampled cores and their microstructures, probably associated with the large-scale faults inferred from interpretations of seismic survey. Rb–Sr isochron, ^{40}Ar–^{39}Ar total gas, and K–Ar ages are largely consistent indicating late Mesoproterozoic and early Proterozoic episodes (~1115 ± 26 Ma, ~1070 ± 25 Ma, ~1040 ± 24 Ma, ~1000 ± 23 Ma, and ~905 ± 21 Ma) of active tectonics in north-central Australia. K–Ar results show that illites from fault gouges and authigenic matrix illites in undeformed adjacent sandstones precipitated contemporaneously, indicating that advection of tectonically mobilised fluids extended into the undeformed wall rocks above or below the fracture and shear (fault gouge) zones. Isotopic age data clearly indicates a Mesoproterzoic minimum age for the Millungera

Basin and thus a previously unrecorded late Mesoproterozoic – early Neoproterozoic tectonic events in north-central Australia. This study provides insight into the enigmatic time-space distribution of Precambrian tectonic zones in central Australia, which are responsible for the formation of a number of sedimentary basins with significant energy and mineral resources.

Keywords: Fault gouge; illite; micro structure; fluid flow; isotope dating; Precambrian; Australia.

1. INTRODUCTION

Direct dating of brittle faulting is crucial for determining the absolute timing of inscrutable time-space distribution of tectonothermal events in concealed Precambrian terranes. Over the last decade, dating of illitic clay from near-surface fault gouges has increasingly become a routine approach to defining the timing of brittle deformations (van der Pluijm et al., 2001; Uysal et al., 2006; Mutlu et al., 2010; Zwingmann and Mancktelow, 2004, Zwingmann et al., 2010; Duvall et al., 2011; Hetzel et al., 2013, Torgersen et al., 2014; Mancktelow et al., 2016, Viola et al., 2016; Algea et al., 2019; Babaahmadi et al., 2019). This technique has been particularly useful in better understanding the development of convergent plate boundaries and continental collisions (e.g., van der Pluijm et al., 2001; Duvall et al., 2011; Isik et al., 2015; Algea et al., 2019; Babaahmadi et al. 2019), movements along transform plate margins (Uysal et al., 2006; Mutlu et al., 2009; Boles et al., 2015), and the formation of orocline bending accompanied by regional strike-slip faulting (Rosenbaum et al., 2015).

While fault gouges reported by earlier studies were mainly from surface outcrops, dating of concealed fault systems is more challenging due to the lack of direct structural observations. Although unknown fault systems buried under thick sedimentary basins can be denoted by geophysical techniques such 2D and 3D seismic reflections, cores from boreholes

48 or tunnel sites intersecting fault zones can be used to date fault reactivation episodes (e.g.,
49 Viola et al., 2013; Yamasaki et al., 2013, Elminen et al., 2018). The current study
50 investigates fault rocks and the host sandstone intersected in drill cores from the newly
51 discovered Millungera Basin in north Queensland, north-central Australia (Fig. 1). It
52 demonstrates how illite geochronology in combination with microstructural and
53 mineralogical studies can be used to reveal a concealed, previously unrecorded Proterozoic
54 tectonic events. Prior to this study (Fig. 1), almost no geological information was available on
55 the Precambrian geology of large parts of north-central Australia, including the Millungera
56 Basin, except for some regional geophysical data (Korsch et al., 2011, 2012) (Fig. 1). This is
57 due to an extensive cover of sediments of the Jurassic–Cretaceous Eromanga-Carpentaria
58 Basin (Fig. 1). Further uncertainties in tectonic interpretation of Australian Precambrian
59 terranes arises from the tendency for original tectonic information to be masked by younger
60 tectonics. Therefore, a major objective of this study was to provide insight into the enigmatic
61 time-space distribution of Mid- to Late- Mesoproterozoic tectonic zones in central Australia,
62 which are responsible for the formation of a number of sedimentary basins with significant
63 potential for energy and mineral resources (Korsch et al., 2011, 2012).

64 Many previous studies have largely focussed on shallow crustal faults that form at
65 diagenetic temperatures below 200°C. Fault gouges from such environments are assumed to
66 consist of (1) detrital illite/muscovite ($2M_1$) derived from wall rocks and (2) authigenic or in
67 situ illite ($1M/M_d$) precipitated within the brittle fault zone during faulting (van der Pluijm et
68 al., 2001; Duvall et al., 2011). Based on a two-end member mixing model, quantified
69 percentages of each illite polytypes (1M and $2M_1$) in different clay size fractions and their
70 apparent ^{40}Ar–^{39}Ar ages are used to extrapolate the age of the pure authigenic illite-$1M/1M_d$
71 polytype (IAA: Illite Age Analyis approach, e.g., van der Pluijm et al., 2001; Duvall et al.,
72 2011). However, assuming that $2M_1$ illite is systematically of detrital origin can be

misleading, since the formation of authigenic $2M_1$ illite in diagenetic-to-hydrothermal conditions is also reported in the literature (e.g, Lonker and Gerald, 1990; Clauer and Liewig, 2013) and brittle faulting can produce authigenic 2M1 illite particularly in areas of elevated geothermal gradients or deeper parts of exhumed faults (Zwingmann et al., 2010; Viola et al., 2013; Mancktelow et al., 2015). While successful isotopic dating of brittle faulting within single fault core was reported previously (Viola et al., 2013), the present study integrating fault rocks from different depths and locations is a new and challenging approach to help better understand illite crystallisation in gouge during relatively low-temperature brittle fault reactivation episodes in complex Precambrian tectonic settings.

2. GEOLOGICAL SETTING, SAMPLE LOCATIONS AND SAMPLING

2.1. Regional tectonic history

The study area, the Millungera Basin is located in northwest Queensland, Australia (Fig. 1a). The Millungera Basin is surrounded by the Paleoproterozoic to Mesoproterozoic Mount Isa Province to the west and Neoproterozic – Ordovician Georgina Basin to the southwest, which developed along the eastern margin of the Proterozoic North Australian Craton. Proterozoic Australia comprises three main tectonic units including the North, West, and South Australian cratons. These units were independently accreted from older crustal fragments by ~1830 Ma (Myers et al., 1996). The North Australian craton has Archean and/or early Paleoproterozoic cores that has been superimposed by later Paleoproterozoic orogenic belts and basins (1800 – 1575 Ma) such as the Mount Isa and Etheridge provinces (Scott et al., 2000; Withnall et al., 2013) (Fig. 1a). The Mount Isa Province is a world-class mineralised terrain with large deposits of copper, lead and zinc, recording polyphase deformation and a multistaged metamorphism that affected the terrane during the Isan Orogeny between 1600 and 1500 Ma (O'Dea et al. 1997).

Australian continental fragments amalgamated as an early component of the Rodinean supercontinent between ~1300 Ma and 1100 Ma (de Vries et al., 2008; Li et al., 2008). The North Australian Craton was first joined to the northwestern margin of the West Australian Craton. The combined West and North Australian cratons were joined to the South Australia Craton along the Albany-Fraser Orogen. The Musgravian Orogen in central Australia was responsible for substantial crustal thickening and high-grade metamorphism at ~1200- 1150 Ma associated with granite intrusion (Evins et al., 2010; Kirkland et al., 2013). Thereafter, uplift and erosion were followed at ~1080 Ma by the deposition and of post-tectonic volcanism, accompanied by the intrusion of widespread plutons (Giles Complex) during the extension along the former collision zones (Schmidt et al., 2006; Evins et al., 2010; Aitken et al, 2013). At the same time, major swarms of dolerite intrusion (e.g., the Lakeview Dyke) were emplaced into the North Australian Craton in the Mount Isa Province (Tanaka and Idnurm, 1994).

During the Neoproterozoic an extensive intracratonic basin (Centralian Superbasin) developed over the junction between the North, South, and West Australian cratons. This was followed by the Rodinia breakup with a mantle plume that initiated continental rifting (Walter et al., 1995; Li et al., 1999). Rodinia breakup resulted in generation of a number of fault-bounded sedimentary basins. It has been proposed that initial period of extension occurred at about 900 Ma and was associated with igneous activities (e.g., Stuart dyke swarms, Black et al., 1980) and intracratonic basin formation in central-north Australia (e.g., Amedeus Basin, Korsch and Lindsay, 1989; Shaw et al., 1991). The Georgina Basin locating in close proximity to the Milungera Basin (Fig. 1a) represents another intarcratonic basin, which consists predominantly of Late Neoproterozoic, Cambro-Ordovician, and Devonian strata unconformably overlying Proterozoic crystalline basement (Shaw et al., 1991; Greene, 2010). The oldest sedimentary unit of the basin is considered to be ~825 Ma (Green, 2010

and references therein). The southern Georgina Basin was deformed during mid-Paleozoic Alice Springs Orogeny, whereby the Neoproterozoic normal faults of the rift basin were reactivated, which are now expressed as high-angle reverse faults (Green, 2010).

2.2. The Millungera Basin and sampling

The Millungera Basin is a recently discovered sedimentary basin in north Queensland, Australia (Korsch et al., 2011, Fig. 1a). It occurs to the east of the Paleoproterozoic Mount Isa Province and is covered by the thin Jurassic–Cretaceous Eromanga-Carpentaria Basin (Fig. 1b). An angular unconformity between the Eromanga and Millungera Basins indicates that the upper part of the Millungera Basin was eroded prior to deposition of the Eromanga-Carpentaria Basin (Korsch et al., 2011) (Fig. 1b), allowing sampling of the deeper part of the basin consisting of flat-lying to gently dipping sedimentary strata (Fig. 1b), which is strongly deformed and faulted (see below). A marked angular unconformity is also interpreted between the basement of the granite and metasedimentary basement rocks and the base of the Millungera Basin (Fig. 1b) Interpretation of gravity profiles indicates that the basin deepens to the south, with a possible maximum thickness of 4,000 m subsurface. Interpretation of aeromagnetic data suggests that the basin might have a dimension of up to 280 km by 95 km (Korsch et al., 2011). Apart from geophysical data, almost no geological information exists on the basin. Prominent thrust fault systems truncate both the western and eastern margins of the basin. Particularly the eastern part of the basin has been cut by several deep-penetrating, northeast-dipping thrust faults, with associated development of hanging wall anticlines. Based on SHRIMP U-Pb geochronology of detrital zircons from the Millungera Basin sandstones, the maximum depositional age of the Millungera Basin is constrained to 1574 ± 14 Ma (Neumann and Kositcin, 2011); however, it is a minimum age and not well constrained between the Cretaceous (overlying sediments) and Mesoproterozoic.

146 Core samples were taken from the lower parts of boreholes Julia Creek 1 (JC) and
147 Dobbyn 2 (Dob) drilled as part of a state (Queensland)-wide geothermal investigation. The
148 wells are 150 km apart (Fig. 1a and Table 1) and intersect the Mesozoic Eromanga-
149 Carpentaria Basin in the upper part. Julia Creek 1 intersected 320.05m of the Eromanga Basin
150 sequence and 179.97m of the Millungera Basin sequence; Dobbyn 2 intersected 332.40m of
151 the Carpentaria Basin sequence and 155.64m of the Millungera Basin sequence. It should be
152 noted that the succession within the Millungera Basin has not been formally defined.
153 According to deep seismic reflection survey, a number of large-scale structures are
154 interpreted to occur as basin-bonding and intra-basin fault systems (Fig 1a-b) (see Korsch et
155 al., 2011). Small scale faults and fractures have also been described from logging of the cores
156 extracted from JC and Dob (Faulkner et al., 2012; Fitzell et al., 2012). We collected a total of
157 9 Julia Creek 1 and 6 Dobbyn 2 fault gouge samples that were all analysed for the <2 μm clay
158 mineral content (Table 1; Supplementary Fig. S1) and some of which have been selected for
159 K–Ar, ^{40}Ar–^{39}Ar, and Rb–Sr dating and trace element studies. We also sampled
160 representative host rock samples adjacent to the fault gouge zones (Table 1).

161 ## 3. ANALYTICAL PROCEDURES

162 ### 3.1. Clay characterisation

163 Samples were prepared for clay-fraction separation by gently hand-crushing the rocks to
164 sand size to avoid artificially reducing grainsize of detrital/primary mineral components and
165 then washed thoroughly by deionised water. Samples were then disaggregated in distilled water
166 using an ultrasonic bath. Clay fractions were separated by the sedimentation method (for <2
167 μm) and centrifugation (for <1 μm subfractions to <0.1 μm). Oriented slides were prepared by
168 pipetting the suspension onto a 30mm × 30mm glass slide to give a concentration of about 3
169 mg/cm^2 or more (Warr and Rice, 1994). XRD on whole-rock samples and clay separates of

different size fractions were carried out (Table 1). The XRD analyses were conducted on a Bruker D4 Endeavor and D8 Advance (CoKα and CuKα radiation, respectively), operated at 40 kV and 30 mA at a scanning rate of 1°2θ/min and 0.05°/step. Following XRD analysis of air-dried samples, the oriented clay-aggregate mounts were placed in an ethylene–glycol atmosphere at 30–40°C overnight prior to additional XRD analyses. For polytype analyses, clay fractions of random powder from fault gouge samples (if sufficient amount of material was available) were scanned from 16 to 44 °2θ in the step-scanning mode with a step size of 0.05 degrees and a counting time of 30 second per step.

Illite polytypes for randomly oriented pure illite samples have been distinguished with the diagnostic peaks suggested by Grathoff and Moore (1996). To determine the $2M_1$ and $1M$ and $1M_d$ % contents of illite/muscovites, the ratios of (2.80 Å – 3.0 Å)/(2.58 Å) and (3.07 Å)/(2.58 Å) peak areas for $2M_1$ and $1M$, respectively were used, as proposed by Grathoff and Moore (1996). The presence of $1M_d$ illite was detected by the presence of the illite hump around the illite 003 diffraction peak (Grathoff and Moore, 1996). WINFIT decomposition by profile fitting was used for determination of areas of the specific peaks of polytypes. Polytype absolute quantification errors are estimated at about ±5%.

The Kübler index (KI) determinations, is defined as the width of the first order illite basal reflection (10Å peak) at half height (FWHM) and expressed in Δ2θ values. The Kübler index decreases with increasing illite crystallinity (a measure of the ordering/ thickness of illite crystallites), with temperature being the most important controlling factor (Ji and Browne, 2000 and references therein). KI is a well-accepted mineralogical indicator of anchizone, hydrothermal and low-temperature regional metamorphism and thermal conditions during fault activity (Merriman and Frey, 1999; Ji and Browne, 2000; Bense et al., 2014).

193 However, Arkai Index (AI) is becoming an additional or alternative technique
194 (particularly in mafic rocks) to evaluate paleotemperature conditions (Árkai, 1991; Warr and
195 Cox, 2016). The AI is determined through measurement of chlorite 002 peak width (Arkai,
196 1991). The KI and AI results of this study were calibrated against the Crystallinity Index
197 Standard (CIS) scale using the procedure and interlaboratory standards of Warr and Mählmann
198 (2015).

199 **3.2. Petrographic analysis**

200 The thin sections were first examined under plane-polarized light and cross-polarized
201 light conditions using a Nikon Eclipse LV100N POL and a Zeiss Axio Imager.A2m polarizing
202 microscope. Further examination of the thin sections was undertaken using a Philips XL 40
203 scanning electron microscope (SEM) equipped with a X-ray energy-dispersive spectrometry
204 (EDS) system for chemical spot analyses. The sections were analysed using 30 kV accelerating
205 voltage and a working distance of 12 mm. Images were collected in back-scattered electron
206 mode. Additionally, clay separates were carbon coated and examined using an EDS equipped
207 Zeiss Ultra Plus SEM qualitative phase identification. The samples were analysed under high
208 vacuum with a 15 kV accelerating voltage and a working distance of 6 mm. Images of clay
209 separate were collected in secondary electron acquisition mode.

210 **3.3. Rb–Sr illite dating**

211 For the Rb–Sr dating (conducted at the Radiogenic Isotope Facility laboratory RIF, the
212 University of Queensland (UQ)), illitic clay separates were leached for 15 min at room
213 temperature in 1 N distilled HCl (Clauer et al., 1993). Leachate and residue were separated by
214 centrifuging. The residue was rinsed repeatedly with milli-Q water, dried and reweighed. Acid
215 leached residues and untreated samples were measured directly by Thermo X-series 1
216 quadrupole ICP–MS with precision better than 0.5% (1σ). The Sr-enriched fraction was

separated using cation exchange resins. Sr isotopic ratios were measured on a VG Sector-54 thermal ionisation mass spectrometer (TIMS. Sr was loaded in TaF_5 and 0.1 *N* H_3PO_4 on a tantalum or tungsten single filament. Sr isotopic ratios were corrected for mass discrimination using $^{86}Sr/^{88}Sr = 0.1194$. Long-term (6 years) reproducibility of statically measured NBS SRM 987 (2σ; $n = 442$) is $^{87}Sr/^{86}Sr = 0.710249 \pm 0.000028$. More recent dynamically measured SRM 987 had $^{86}Sr/^{88}Sr$ ratios of 0.710222 ± 0.000020 (2σ; $n = 140$). Rb–Sr isochron ages were calculated using the ISOPLOT program (Ludwig, 2012) and decay constant recomented by Villa et al. (2015). For isochron age calculation, standard errors of ±0.01% for $^{87}Sr/^{86}Sr$ and of ±1% for $^{87}Rb/^{86}Sr$ ratios were assigned to the results. Individual analytical uncertainties were generally smaller than these values.

3.4. K–Ar illite dating

The K–Ar dating was performed at the CSIRO Argon facility in Perth, Australia according to standard methods given in detail by Dalrymple and Lanphere (1969). Potassium content was determined by atomic absorption. The error of K determination of standards is better than 1.2% 1σ. The K blank was measured at 0.50 ppm. Argon was extracted from the separated mineral fraction by fusing the sample within a vacuum line serviced by an on-line ^{38}Ar spike pipette. The isotopic composition of the spiked Ar was measured with a high sensitivity, on-line, VG3600 mass spectrometer. The ^{38}Ar was calibrated against standard biotite GA1550 (McDougall and Roksandic, 1974). Blanks for the extraction line and mass spectrometer were systematically determined and the mass discrimination factor was determined periodically by airshots (small amounts of air for $^{40}Ar/^{36}Ar$ ratio measurement). During the course of the study, 16 international standards (8 HD-B1 and 8 LP-6) and 16 airshots were analyzed. The results are summarized in Table 2. The error for the $^{40}Ar/^{36}Ar$ value of the airshot yielded 296.08 ±1.23, (0.41%) 1σ.. The general error for argon analyses is below 1.3% (1σ) based on the long-term precision of 330 measurements of international Argon standards..

242 The K-Ar age was calculated using ^{40}K abundance and decay constants recommended by
243 Steiger and Jäger (1977). The age uncertainties take into account the errors during sample
244 weighing, $^{38}Ar/^{36}Ar$ and $^{40}Ar/^{38}Ar$ measurements and K analysis.

245 **3.5. ^{40}Ar–^{39}Ar illite dating**

246 Four fault gouge illites were dated by the ^{40}Ar–^{39}Ar method at the University of
247 Michigan. Illitic clay samples were re-suspended in 1 ml of deionized water, spun-down at
248 10,000 rpm in a microcentrifuge and carved into a ~1 mm pellet following decanting. To avoid
249 loss of ^{39}Ar due to recoil, clay pellets were placed in 1 mm ID fused silica vials prior to being
250 sent for neutron irradiation for 90 MWh in medium flux locations of the McMaster Nuclear
251 Reactor (hole 8C for irradiation 1, 8A for irradiation 2). Following irradiation, samples were
252 attached to a laser fusion system, the vials were broken under a 1 x 10–8 Torr vacuum, and the
253 samples step-heated in situ using a defocused beam from a 5 W Coherent Innova continuous
254 Ar-ion laser operated in multi-line mode. Argon isotopes were then analyzed using a VG1200S
255 mass spectrometer equipped with a Daly detector operated in analogue mode using methods
256 by Hall (2014). Ages in this study are calculated relative to an age of 520.4±1.7 Ma for standard
257 hornblende MMhb-1 (Samson and Alexander, 1987). The total gas age obtained from the
258 vacuum encapsulated sample is equivalent to a conventional K–Ar age and quoted at 1σ.

259 **3.6. Illite trace element analysis**

260 For trace element analysis conducted in the Radiogenic Isotope Laboratory at the
261 University of Queensland (RIF, UQ), clay samples were dissolved with a mixture of HF and
262 nitric acids on a hotplate, then evaporated to dryness, refluxed twice with nitric acid and
263 dissolved in 2N nitric acid. Aliquots of the solutions were spiked with internal standards,
264 diluted and analysed on a Thermo X-series 1 quadrupole inductively coupled plasma mass
265 spectrometer (ICP-MS). Sample preparation and analytical procedures used were similar to

266 those of Eggins et al. (1997), except that Tm was not used as an internal standard and duplicate
267 low-pressure digestions of US Geological Survey W-2 diabase standard and a known
268 concentration profile (pre-analysed by laboratory) were used for calibration (Li et al., 2005). .
269 The $^{156}CeO/^{140}Ce$ ratio for the run was 0.016. Long-term precision (RSD) was based on
270 duplicate analyses of the duplicate digestions of AGV1, whilst precision for the run was based
271 on five duplicate analyses of W-2 which were better than 3% for most elements, except for Li,
272 Zn, Mo, Cd, and Cs, which ranged between 5% (Li, Cd and Cs) and 15% (Zn).

273 # 4. RESULTS

274 ## 4.1 Sample description and micro structures

275 *4.1.1 Core descriptions*

276 The undifferentiated Millungera sequence intersected in Julia Creek 1 and Dobbyn 2
277 comprises medium to coarse-grained, pink to dark red quartzose sandstone with minor
278 interbeds of micaceous clay siltstone and claystone. These sandstone intervals are fractured
279 and faulted throughout the sequence and show evidence of pervasive hydrothermal alteration,
280 particularly near the cracks (Fig. 2a, see also Faulkner et al., 2012; Fitzell et al., 2012).
281 Alteration products are very fine-grained clay-rich material that contain angular clasts from
282 the main rock (Fig. 2b). Clay-rich layers show mostly different colour (grey-beige-red)
283 relative to the sandstone wallrock (Fig. 2b-e). Numerous open cracks coated with green clay
284 are observed throughout cores (Fig. 2c). The clay rich material occurs along the fault planes
285 and in cracks as single vein or complex network of partially consolidated material (Fig. c-d).
286 They also exist as relatively thick layers (up to 30 cm) within the sandstone cores (Fig. 2e),
287 with a sharp transition the host rock (Fig. 2a-f) and contain commonly slickenside surfaces at
288 the contact with the host rock (Fig. 2f-h).

289 *4.1.2 Petrographic and micro-structural analysis*

290 Thin section photomicrographs and SEM images of representative samples are shown
291 in Fig. 3a-f. Microscopic observations show that the undeformed host rock sandstones consist
292 of mainly quartz, some muscovite and minor K-feldspar. Petrography, in combination with
293 XRD analysis show that kaolinite, illite, and chlorite are present as a pore and fracture-filling
294 cement in the sandstones (Fig. 3a-b), while detrital mica occurs in large elongate grains with
295 alteration in illite along its edges (Fig. 3b-c). Chlorite does not show any coarse detrital
296 grains and only occurs authigenetically in very fine-grains dispersed and mixed with illites as
297 pore-filling mineral phases (Fig. 3a).

298 Faulted specimen from Julia Creek 1 show a characteristic S-C foliation (e.g. Berthe et
299 al., 1979) under the optical microscope (Fig. 4a, b and c) with an anastomosing network of
300 phyllosilicate defining the C shear oriented parallel to the shear direction. The S- shears
301 include planes of insoluble minerals oriented oblique to the sense of shear (Fig. 4c) and
302 quartz fragments embedded in a fine-grained illite-rich matrix as shown by electron
303 microscopy imaging (Fig. 4d and e). These quartz grains have angular shape with intensely
304 serrated grain boundaries and are slightly elongated with their long axis parallel to the
305 orientation of the S- surface. Booklets of kaolinite partially replaced by illite are also visible
306 in the deformed specimens (e.g. Fig. 4d and e).

307 Faulted hand specimens from Dobbyn 2 exhibit planar to slightly arcuate fault surfaces
308 with a high gloss and display evident slickenside surfaces decorated by short-wavelength
309 (200-500 μm) striations (Fig. 5a). Sense of shearing and offset on the faults are difficult to
310 assess due to lack of markers visible in the cores. Domains of foliated and brecciated
311 cataclasite can be distinguished on hand specimen (Fig. 5b) and in thin section (Fig. 5c). Both
312 domains are characterised by hematite rich injection veins emanating from the slip surfaces

313 and oriented at approximately right angle to them with sharp contacts with the surrounding
314 material (Fig. 5 d, e). The domains are bounded by sharp contacts defined by slickenside
315 surfaces constituted by thin layers (50-100 μm thick) of iso-oriented phyllosilicates (Fig. 5d,
316 f). The foliated cataclasite domains are characterised by a set of conjugate shears referred to
317 as S-C-C' structures visible at the micro-scale using scanning electron microscopy (Fig. 5e).
318 Oblique to the shear direction S surfaces are defined by the preferred alignment of elongated
319 phyllosilicate minerals and are oriented approximately perpendicular to the maximum
320 flattening of the strain ellipsoid.

321 C and C' represent discrete shear surfaces, the former is parallel to the macroscopic slip
322 surface and the latter deflects the S foliation by disrupting the grains into a plane composed
323 of ultrafine comminuted grains oriented at a small angle (~ 20°) to the macroscopic shear
324 surface but with the opposite sense of obliquity relative to the S-surfaces (Fig. 5e). The
325 cataclasite domain show the original rock fabric of detrital quartz grains and pore-filling
326 diagenetic kaolinite disrupted by a pervasive network of hematite filled intragranular micro-
327 fractures (Fig. 5g).

328 *4.1.3. XRD and SEM clay mineral analysis*

329 Illite is the most abundant clay mineral in the majority of samples, with kaolinite and
330 chlorite being present in many samples. The latter minerals are more abundant than illite in
331 sample Dob-449.3 (Table 1; Supplementary Fig. S1). XRD analysis shows that 001 peak
332 position of the illite does not change after ethylene glycol treatment, which indicates that
333 smectite-like clays are not present or their amount is insignificant (Srodon and Eberl, 1984).
334 There is also no noticeable change in KI values after the ethylene glycol treatment of the
335 samples. KI measurements for <2 μm size fractions normalised to the standards of Warr and
336 Rice (1994) range from 0.17 to 1.00 $\Delta^{o}2\theta$ and from 0.46 to 1.01 $\Delta^{o}2\theta$ for samples from

Dobbyn 2 and Julia Creek 1, respectively (Table 1). We also measured KI values of >2 μm size fractions of some fault gouge samples. Such non-clay fractions contain mostly parallel-oriented mica-type inherited/detrital minerals representing the pre-fault protolith. Coarser (>2 μm) size fractions of samples JC-408, Dob-441, Dob-449.3, and Dob-476.6 KI give values of 0.42 *Δ°2θ,* 0.36 *Δ°2θ*, 0.14 *Δ°2θ*, and 0.26 *Δ°2θ*, respectively, whereas <2 μm fractions of the same samples provide considerably higher KI values of 0.60 *Δ°2θ*, 0.42 *Δ°2θ*, 0.19 *Δ°2θ*, and 0.33 *Δ°2θ*, respectively. KI values of < 2 μm size fractions of the host rock range between 0.18 and 0.23 *Δ°2θ,* and 0.46 and 0.68 *Δ°2θ* for Dobbyn 2 and Julia Creek 1 samples, respectively (Table 1). The normalised chlorite crystallinity values (AI) of <2 μm for samples free of kaolinite range from 0.35 to 0.42 *Δ°2θ* (Table 1).

Non-oriented random powder XRD analysis of <2 μm, 2-1 μm, <1 μm, and <0.5 μm fractions for samples from borehole Julia Creek 1 (JC) confirm the mixture of $2M_1$, 1M, and$1M_d$ polytypes of illite, while samples from borehole Dobbyn 2 consist of largely $2M_1$ illite with some $1M_d$ illite up to 20% for some samples (Table 1, Supplementary . S1). SEM analysis of <2 μm fractions show $2M_1$ illites forming large euhedral crystal plates with sharp edges that occur together with smaller $1M/1M_d$ illite plates (Fig. 3c-f). A number of previous studies (e.g., Clauer and Liewig, 2013) showed that detrital illitic clay particles rarely have straight edges, but rather occur in particles with diffuse-blurred and irregular edges (Fig. 3c, like the white material on the right-hand site). Samples Dob-441 and Dob-476.6 have generally larger crystal size (Fig. 3c-d) than samples JC-408 and JC-360.7 (Fig. 3c-d). The abundancy of $2M_1$ illite represented by these larger crystal plates in samples Dob-441 and Dob-476.6 is confirmed by XRD random powder polytype analysis (Table 1; Supplementary Fig. S1). Dob samples however, are poorly sorted in terms of crystal size distribution with the presence of a number of much smaller crystals (Fig. 3c-d). Such small crystals are mostly rounded (see the arrow in Fig. 3d).

362 **4.2. Illite geochronology**

363 *4.2.1. ^{40}Ar–^{39}Ar dating*

364 Four fault gouge illite samples of <2μm fraction were analysed for ^{40}Ar–^{39}Ar
365 geochronology (Table 1 and Fig. 6). Based on their illite crystallinity values, these samples
366 represent deep diagenetic to upper anchizonal metamorphic grade with 2M1 illite varying
367 between 62% and 100%. Samples had 5%–12% low temperature ^{39}Ar recoil loss, which is
368 characteristic of well crystallised illite grains (Hall et al., 1997). Age data (1σ) are obtained
369 as total gas ages (Table 1 and Fig. 6) (cf., Dong et al., 1995). Samples JC-360.7, JC-408,
370 Dob-441, and Dob-446.6 yield total gas of 1038.1 ± 2.9 Ma, 1040.0 ± 2.3 Ma, and 1068.1±
371 1.8 Ma, and 994.6 ± 2.2 (Table 1; Fig. 6). The analyses do not show well developed
372 plateaux, which can be explained by recoil and varying ages of individual crystals (cf., Clauer
373 et al., 2012).

374 *4.2.2. K–Ar dating*

375 K–Ar ages of fault gouge and sandstone illites of different size fractions from >2 μm to
376 <0.1 μm from boreholes Julia Creek 1 and Dobbyn 2 are presented in Table 1 and Fig. 7. A
377 histogram of all K–Ar results obtained from gouge zones are shown in Fig. 7a. K–Ar size
378 fraction ages for fault gouge and host rock matrix illite and their interpretation in relation to
379 the tectonic history are shown in Fig. 7b and Fig. 7c, respectively. Due to sample nature it
380 was not possible to extract sufficient material for <0.1 μm or <0.5 μm fractions from some
381 fault rock samples, especially from those samples from Dobbyn 2 with illites with low KI
382 values (0.42 $\Delta 2\theta$ or lower for <2 μm).

383 Size fractions from <2 μm to <0.1 μm of fault gouge samples JC-343, JC-360.7, and
384 JC-440.5 from Julia Creek 1 yield consistent ages (Table 1) with a mean (average) of 1036.2

385 ± 9.7 Ma, 1025 ± 17.7 Ma, 1028.9 ± 17.3 Ma (1 s.d.), respectively. The mean age of 1025 ±
386 17.7 Ma for sample JC-360.7 is identical with the Ar–Ar total gas age of 1038.1±2.9 Ma of
387 <2 μm of the same sample. Various size fractions from 2-1 μm to <0.5 μm of another fault
388 gouge sample from Julia Creek 1 (JC-408) give also consistent but older ages with a mean of
389 1114.2 ± 6.9 Ma. However, a younger ^{40}Ar–^{39}Ar total gas age of 1040.0 ± 2.3 Ma is obtained
390 for <2 μm fraction of sample JC-408 (Table 1; Fig. 6). The >2 μm fraction of sample JC-408
391 yields, by contrast, a distinctively different and older K–Ar of 1243.2 ± 29.1 Ma (Table 1).

392 K–Ar ages of different fault gouge illites from Dobbyn 2 are more variable (Fig. 5a). 2-
393 1 μm, <2, 1-0.5 μm, and 0.5-0.1 μm fractions of sample Dob-389.6 yield consistent ages
394 (Table 1; Fig. 7b) with a mean of 1061 ± 19.5 Ma, whereas <0.5 μm and <0.1 μm give
395 younger ages of 981.8 ± 22.6 Ma and 905.4 ± 20.9 Ma, respectively.

396 Smaller 2 and <1 μm fractions of fault sample Dob-441 give inconsistent but close K–
397 Ar ages of 1148.7 ± 26.9 Ma and 1086.5 ± 25.1 Ma, respectively. The ^{40}Ar–^{39}Ar total gas age
398 of 1068.1 ± 1.8 Ma for this sample is consistent with the K–Ar age of 1086.5 ± 25.1 Ma of
399 the <1 μm fraction. A significantly older K–Ar age of 1312.3 ± 30.7 Ma is obtained for the
400 >2 μm fraction of sample Dob-441 (Table 1; Fig. 7b).

401 Samples Dob-449.1 and Dob-449.3 were taken from a clay-rich fault rock zone, with
402 the former and latter representing beige-light grey and hematite-rich red varieties,
403 respectively. The 2-0.5 μm, <2 μm, 1-0.5 μm, and <0.5 μm fractions of sample Dob-449.1
404 yield younger but concordant ages with a mean of 922.4 ± 19.9 Ma. However, illite fractions
405 of sample Dob-449.3 (just 20 cm below) yield scattering K–Ar ages regardless of the grain
406 size. K–Ar ages of size fractions 2-1 μm, 1-0.5 μm, 0.5-0.2 μm, and <0.5 μm for sample
407 Dob-449.3 are 1047.7 ± 24.2 Ma, 1117.2 ± 25.8 Ma, 950.9 ± 22.0 Ma, and 1004.4 ± 23.2 Ma,

408 respectively. Coarser > 2 μm fraction being rich in detrital mica gives a much older age of
409 1259.0 ± 29.1 (Table 1; Fig. 7b).

410 K–Ar age of 2-1 μm fraction and K–Ar and ^{40}Ar–^{39}Ar total gas ages of <2 μm fraction
411 of the deepest fault rock sample from Dobbyn 2 (Dob-476.6) yield identical ages within
412 analytical errors of 975.7 ± 22.2 Ma, 983.7 ± 23.0 Ma, and 994.6 ± 2.2 Ma, respectively, with
413 a mean of 984.7 ± 9.5 Ma. A much older age of 1170.4 ± 27.4 Ma is obtained for >2 μm
414 fraction of this sample (Table 1; Fig. 7b).

415 K–Ar and ^{40}Ar–^{39}Ar results of all size fractions (except >2 μm) from fault gouges listed
416 in Table 1 are presented as a histogram and probability density distribution plot (Fig. 7a).
417 Isotopic dates define distinct age clusters at ~1070 Ma, ~1040 Ma, and ~995Ma. There are
418 also less pronounced, but noticeable age clusters at ~1115 Ma and ~905 Ma (Fig. 7a).

419 K–Ar ages of different size fractions of illitic clay minerals that occur as matrix in
420 undeformed, adjacent sandstones (see Figs. 2 and 3) are also presented in Table 1 and Fig. 7c.
421 Three different size fractions of three different samples, Dob-449.4, JC-500, and JC-360.6,
422 yield same ages within error, averaging at 1047 ± 21 Ma, 1079 ± 13 Ma, 1062 ± 7 Ma (1 s.d),
423 respectively (Table 1 and Fig. 7c). The <0.2 fine fractions of JC-360.6 and JC-500 yield
424 within error identical younger agers of (928.3 ± 47.6 and 878.3 ± 45.1, respectively), which
425 might indicate cessation of illite formation or partial reset due to final faulting with the Early
426 Neoproterozoic deformation events and associated fluid flow.

427 *4.2.3. Rb–Sr isochron dating*

428 Rb–Sr data for the untreated, acid-leached residues, and leachates of different <2μm
429 clay fractions for the fault gouge illites collected from different stratigraphic levels in Julia
430 Creek 1 and Dobbyn 2 are presented in Table 3 and on Fig. 8. The data show three parallel

well-defined linear relationships indicating similar isochron ages, but with different initial $^{87}Sr/^{86}Sr$ values (Fig. 8a). Some samples plot between these lines (Fig. 8a), possibly because they have different initial $^{87}Sr/^{86}Sr$ values, and these samples are not considered for isochron age calculation. Samples from Dobbyn 2 plot on the two upper isochron lines with higher $^{87}Sr/^{86}Sr$ initial values (Fig. 8a). Residue of samples JC-360.7B<0.5 μm plot also on one of these lines (the middle line on Fig. Fig. 8a). All other Julia Creek 1 define a separate Rb–Sr isochron line with lower $^{87}Sr/^{86}Sr$ initial values (the lower line on Fig. 8a).

Leachates are accessory acid-soluble non-silicate phases (mostly carbonate minerals and amorphous grain coatings of FeO(OH) (Clauer et al., 1993). However, Rb–Sr isotopic systematics of the acid-soluble leachate is not in equilibrium with that of the illites, since the leachates plot off the Rb–Sr lines. Lower $^{87}Sr/^{86}Sr$ values of the leachates (mostly<0.72) in comparison to highly radiogenic (elevated) initial $^{87}Sr/^{86}Sr$ of of illites indicate interaction of rocks with some late stage fluids from which acid-soluble non-silicate phases were formed.

The data of untreated and residues of <2 μm fractions from Julia Creek 1 samples define a linear relationship from which the slope yields a Rb-Sr errorchron age of 1041 ± 46 Ma (initial $^{87}Sr/^{86}Sr$ = 0.7194±0.0011, MSWD=27) (Fig. 8b). However, as apparent from the $^{87}Rb/^{86}Sr$ vs. $^{87}Sr/^{86}Sr$ plot on the Fig. 8a-b, untreated aliquots of samples JC-387.8 and JC-440.5 plot slightly at the lower part of the line leading to a large analytical error and MSWD value. This is probably caused by the effect of the leachable components that were not in isotopic equilibrium with the clays, as discussed above. When these two untreated samples are omitted, the data scatter is reduced significantly with a well-defined regression line (MSWD=2.3) and corresponding isochron age of 1023 ± 12 Ma (initial $^{87}Sr/^{86}Sr$ = 0.72009±0.00025) (Figure 8c). Residue and untreated aliquots of <2 μm fractions from Dob-449, Dob-441A, and Dob-389.6, and residue of JC-360.7B <0.5 μm yield an analytically

indistinguishable age of 1033 ± 25 Ma (initial $^{87}Sr/^{86}Sr$ = 0.72326±0.00094; MSWD=2.5) (Fig. 8d). A somewhat younger Rb–Sr age of 1000 ± 12 (initial $^{87}Sr/^{86}Sr$ =0.72841±0.00030, MSWD = 0.065) was obtained for Dob-476.6 <2 μm (untreated and residue), Dob-389.6 2-1 μm and 0.5-0.1 μm (residue) (Fig. 8e).

4.3. Trace elements

Rare earth element (REE) data and Th, U, and Sc contents of illites (<2 μm clay-size fractions) from the fault gouge samples are given in Table 4. Chondrite-normalised REE patterns of illites from the fault gouges are shown in Fig. 9a. In addition, the REE pattern of Post-Archean Average Shale (PAAS, Taylor and McLennan, 1985) is included in the REE diagram. The fault gouge illites are substantially enriched in light REE (LREE) relative to PAAS with La contents as high as10xPAAS. The illites are however, somewhat depleted in heavy REE (HREE) relative to LREE (Fig. 9a). The chondrite-normalised $(La/Lu)_c$ ratios of the illites are significantly higher (up to 76) than the $(La/Lu)_c$ ratio of PAAS (10) (Table 4). Fault gouge illites are also enriched in Th and U (up to 10 times) in comparison to PAAS (Table 4).

5. DISCUSSION

5.1. Faulting, fluid-rock interactions and clay generation

Brittle deformation and faulting is evident from cores in the sampled intervals in Julia Creek 1and Dobbyn 2, probably associated with the large scale faults inferred from interpretations of seismic survey (Fig. 1). Under upper crustal conditions, fault zones accommodate intense shear strain often localised in bands of cataclastic deformation formed by friction-dominated faulting within the seismogenic regime (Sibson, 1977; Schmid and Handy, 1991). While cataclastic fault rocks are generally considered to display random

478 fabric, foliated fault rocks such as fault gouge and foliated cataclasites have also been
479 reported in different lithologies ranging from crystalline rocks to siliciclastic and carbonate
480 dominated sediments at different burial or deformation depths (Chester et al., 1985; Rutter et
481 al., 1986; Lin, 1999; Ujiie et al., 2007; Laurich et al., 2004; Delle Piane et al., 2017; Nicchio
482 et al., 2018). Frictional sliding and abrasion are common processes during repeated fault
483 movement and result in strong grain size reduction of the fault rocks with respect to the
484 constituting minerals in the undeformed portion of the host rocks. The abundant presence of
485 micro and nano-sized particles in cataclasites and gouges may result from combined effects
486 of cataclasis and pressure solution-precipitation during deformation in the presence of fluids
487 (e.g. Vrolijk and van der Pluijm, 1999; Solum et al., 2005). Foliated cataclasites have also
488 been observed at very shallow depths in siliciclastic sediments (<500 m, e.g., Balsamo et al.,
489 2014) and carbonate rocks (< 2km; e.g., Smeraglia et al., 2016) as the result of cataclasis,
490 clay smearing and/or pressure solution-precipitation in presence of fluids during deformation.
491 The corroded grain boundaries of quartz grains in faulted samples from Julia Creek 1 (Fig. 4)
492 and the presence of the injection veins and hydrothermal hematite in the cataclasites from
493 Dobbyn 2 (Fig. 5) indicates that deformation occurred in a fluid-rich environment that
494 promoted detrital muscovite dissolution and new growth of illite. The small injections veins
495 that are observed to cut through the foliated cataclasites and the detrital quartz grains (Fig. 5)
496 may represent the effect of hydraulic fracturing due to a fast increment of fluid pressure in the
497 fault zone during a seismic slip (e.g. Sibson, 1989; Cowan et al., 2003; Ujiie et al., 2007;
498 Rowe et al., 2012). At the core scale, some samples show no shearing-related fabrics in the
499 sandstone cores (fresh and hard) adjacent to clay-filled cracks (Fig. 2a-d). This may be a
500 result of the precipitation of clay-rich material and injection of granular material from
501 seismically-mobilised circulating fluids (c.f., Smeraglia et al., 2016).

K–Ar results show that illites from fault gouges and matrix illites in undeformed adjacent sandstones precipitated contemporaneously (Fig. 7). In some tectonically active regions, mineral assemblages from the fault rocks and their parent rocks are significantly different, whereby parent rocks do not contain any alteration minerals with new mineral growth being restricted to the fault rocks. This indicates that the heat and fluid flows associated with mineral authigenesis were not controlled by regional tectonic events in these regions, but rather confined to the areas within the fault zone (e.g., Uysal et al. 2006; Isik et al., 2014; Babaahmadi et al., 2019). However, the relation between large-scale fluid flow and seismic events has long been reported (e.g., Bruhn et al., 1994; Eichhubl et al., 2010; Faulkner et al., 2010; Lupi et al., 2010 and references therein). Brittle faulting in the upper crust involves episodic changes in the stress level that can expel large volumes of fluids, leading to the generation of hydrothermal/geothermal systems (e.g., Maffucci et al., 2016). Faults and veins and their immediate surrounds represent zones of fluid passage and transfer of mass through those fluids (e.g., Sibson, 1987). Mineral alteration in slip zone gouge extends outward from the fault zone into the undeformed wall rock (e.g., Parry et al., 1991; Craw et al., 2009). The wall rock alteration is attributed to the diffusion and advection of fluids, and hence chemical mass and heat transfer associated with deformation. For example, metasomatic alteration zones develop around fluid pathways by advection with mineral dissolution and precipitation increasing towards the conduit and dictated by infiltrating fluids (Ferry and Dipple, 1991; Rossetti et al., 2011; Maffucci et al., 2016). Metasomatic mineral alteration is common in sedimentary basins contemporaneous with regional extensional tectonics. Alteration is driven by reactivity of sandstone host rocks with illitic clay minerals, K-feldspar (adularia), hematite, calcite, and quartz being some common minerals precipitating from tectonically mobilised K-bearing basin brine (Fedo et al., 1995; Michalski et al., 2007; Eichhubl et al., 2010, Rossetti et al., 2011). Similarly, in this study, sandstone

527 immediately above or below the fracture and shear (fault gouge) zones represents zones of
528 alteration of detrital minerals to illite by tectonically moved fluids.

529 **5.2. Geochronology: comparison between K–Ar, ^{40}Ar–^{39}Ar and Rb–Sr ages**

530 Fault gouges from the Millungera Basin in Australia (Fig. 1) contain a mixture of
531 coevally formed 1M/1M_d and 2M_1 illite from which the crystallisation age was determined by
532 a combined application of Rb–Sr, ^{40}Ar–^{39}Ar, and K–Ar techniques. It is demonstrated that
533 applying both the Rb–Sr and K–Ar (^{40}Ar–^{39}Ar) techniques for dating the same fault gouge
534 minerals provides more robust and complementary age constraints on faulting episodes and
535 minimises the inherent disadvantages for each isotopic system. A common drawback of Ar
536 geochronology when dating white mica is that Ar apparent ages are either significantly older
537 or younger than the Rb–Sr isochron ages of the same samples (Kelley, 2002; Di Vincenzo et
538 al., 2006). Rb–Sr isotopic systematics may remain unaffected because Rb–Sr resetting
539 requires higher closure temperatures and sufficient fluids in the system to facilitate
540 recrystallisation (e.g., Di Vincenzo et al., 2006). However, a potential pitfall of Rb–Sr dating
541 technique could result from heterogeneous initial ^{87}Sr/^{86}Sr ratios on a mineral-scale (cf.,
542 Davidson et al., 2005). In this study, as discussed in section in section 4.2.3, we minimised
543 the effect of mineral-scale initial isotopic heterogeneity by analysing different aliquots
544 (untreated, leachates, and residues) and different sub-size fractions of one clay sample.
545 Indeed, different sub-size fractions and aliquots of some samples plot on different isochron
546 lines indicating different ^{87}Sr/^{86}Sr ratios (Fig. 8, see the discussion below). Illites from the
547 Millungera Basin fault gouges display well-developed linear data arrays on Rb–Sr isochron
548 diagrams that we interpret to reflect statistically valid late Mesoproterozoic ages (Fig. 8).

549 Numerous case studies as discussed in detail below indicate that such linear relations
550 can result from either a mixing between different mineral populations with different initial
551 ^{87}Sr/^{86}Sr ratios, or from a complete isotopic equilibration of the entire mineral assemblage at

552 a given time. In the former case, the linear relationship between $^{87}Rb/^{86}Sr$ and $^{87}Sr/^{86}Sr$ could
553 have developed from a mixing line of two end members with potentially no genetic
554 relationship, therefore without meaningful age information, whereas the latter relation
555 provides a valid isochron whose slope yields the age of illitic clay generation during a fault
556 reactivation event. However, valid and geologically significant isochrons and mixing lines
557 can also be obtained simultaneously from samples with different mineral populations,
558 comprising minerals with different Rb/Sr ratios but identical initial $^{87}Sr/^{86}Sr$ ratios. In this
559 case of identical initial Sr-isotopic compositions of two components of a mixture at time t=0,
560 the two components and mixtures thereof define a horizontal line both in a classic isochron
561 diagram (which is the key condition for validity of calculated Rb–Sr isochron ages), and in
562 the $^{87}Sr/^{86}Sr$ vs. $1/^{86}Sr$ diagram commonly used for evaluation of binary isotopic and
563 compositional mixing (cf. Wendt, 1993 and Schneider et al. 2003 for theoretical background).
564 In sedimentary basins or hydrothermal systems, samples with various Rb/Sr ratios can
565 precipitate from a chemically homogeneous basinal fluid that can yield the same isotopic
566 composition across the entire sedimentary basin (e.g., Uysal et al., 2001; Golding et al.,
567 2013). Fault gouge clay separates from the Milungera Basin contain a mixture of illites and
568 other authigenic clay minerals such as chlorite and kaolinite (see the section 4.1.2) and minor
569 carbonates, which include considerable amounts of Sr but no or very little Rb (in contrast to
570 illite). Since samples used for Rb–Sr analysis contain these different minerals in various
571 amounts, the obtained linear relations can be considered to have evolved from (initially
572 horizontal) mixing lines but simultaneously represent geologically meaningful isochron
573 correlations. The isochron ages are consistent with K–Ar ages of the same clay-size fractions
574 of the corresponding samples that provides a further strong support in favour of isochrons
575 with a meaningful age information (see below). Similarly, valid Rb–Sr ages based on linear
576 relations representing both isochrons and mixing lines were commonly obtained from

leachate, untreated, and residue aliquots of fault gouge and matrix illites (Clauer and Chaudhuri, 1995; Mutlu et al., 2010; Uysal et al., 2011; Golding et al., 2013; Isik et al., 2014; Middleton et al., 2014; Rosenbaum et al., 2015; Babaahmedi et al., 2019).

The Rb–Sr isochron ages of JC samples are concordant with K–Ar ages of same samples (Table 1). For example, the Rb–Sr isochron ages (1041 ± 46 Ma and 1023 ± 12 Ma) for <2 μm fractions of samples JC-360.7, JC-440.5 (Fig. 8b-c) are consistent with K–Ar and for ^{40}Ar–^{39}Ar (sample JC-360.7) ages of the same fraction and all other different size fractions of the same samples (Table 1 and Fig. 7). However, K–Ar and Rb–Sr ages are not consistent for a number of Dob samples. K–Ar ages of Dob-389.6 and Dob-441samples are older than the corresponding Rb–Sr isochron ages, while K–Ar ages of all different size fractions for sample Dob-449.1 are lower (925 to 913 Ma) than the Rb–Sr isochron age (Fig. 8b-d, Table 1). The Rb–Sr isochron age of 1000 ± 12 Ma for <2 μm of sample Dob-476.6 (along with the acid-leached residues of Dob-441B and Dob-389.6 for 2-0.5 μm to 0.5-0.1 μm fractions) is consistent with K–Ar ages of the same sample for coarser size fractions (975.7 ± 22.2 and 983.7 ± 23.0 Ma) within analytical errors. <1 μm fraction of sample Dob-476.6 yields a consistent K–Ar age (922.2 ± 21.2) with clays of all size fractions of sample Dob-449.1 (Table 1).

In summary, all JC samples with their various size fractions yield consistent Rb–Sr isochron and individual K–Ar ages. This finding is similar to those reported by some recent studies that presented robust and comprehensive Rb–Sr, ^{40}Ar–^{39}Ar, and K–Ar age data for deep diagenetic and anchizonal fault gauge illites (e.g., Middleton et al., 2014; Rosenbaum et al., 2015; Babaahmadi et al, 2019). Discrepancy in Rb–Sr and K–Ar ages for Dob samples, e.g., Dob-441 <2 μm (K–Ar age is older) and Dob-449.1 (K–Ar ages are younger), and the internal inconsistency of K–Ar ages among different size fractions of sample Dob-4449.3

(e.g., 1048 ± 24 for 2-1μm and 1117 ± 26 for 1-0.5 μm fractions; see Table 1) may result from sample heterogeneity (hand-specimen and micro scale, see Figs. 4 and 5) presented by more than one illite generation due to multiple faulting episodes (see section 5.4).

Mixing of different generations is possible in small scale as a result of variable degrees of isotopic resetting of a single illite generation during subsequent faulting events. Pervasive overprinting and re-crystallization can be hindered even in micro scale, which may result from a lack of permeability and/or limited availability of fluids (e.g., Bröcker et al., 2013).

5.3. Implication of Sr isotope and trace element compositions for the evolution of fault-related fluids

The trace element composition of authigenic clay minerals reflects the mineral/fluid partition coefficients for different elements, as well as the composition of fluids from which the clays precipitated. Trace element contents and concentrations, as well as some element ratios, can be used to trace the origin of basinal and hydrothermal fluids (e.g., Uysal and Golding, 2003; Uysal et al., 2005; Uysal et al., 2011). The fault gouge illites analysed in this study are highly enriched in LREE and other incompatible elements such as Th and U relative to PAAS (Fig. 9a and Table 4). This geochemical characteristic indicates precipitation of the illites from fluids that must have interacted with rocks of the upper crust enriched in incompatible and heat producing elements. This is also consistent with initial $^{87}Sr/^{86}Sr$ values of fault gouge illites that reflect Sr isotope composition of fluids from which the illites precipitated. The radiogenic initial $^{87}Sr/^{86}Sr$ ratios of about 0.72 indicate the involvement of fluids that equilibrated with old Rb-rich crustal rocks. The trace element and Sr isotope data are in agreement with seismic and potential field data by Korsch et al. (2011), which is interpreted as indicating the occurrence of granites with a thickness of up to 5.5 km below the Millungera Basin. The inferred granites may be a part of the granite (Williams

625 Supersuite) exposed just to the west in the Mt Isa Inlier, which is enriched in Th, U, and K
626 (Korsch et al., 2011 and references therein).

627 Different $^{87}Sr/^{86}Sr$ initial values of illites of the parallel isochron lines corresponding to
628 the same Rb–Sr age in Fig. 8 and scatter of Rb–Sr data points for some samples indicate
629 separate circulation pathways for seismically mobilised fluids that that might have restricted
630 to unconnected fault planes and fracture systems in different areas of the Millingera Basin.

631 **5.4. Changes of illite crystallinity in relation to K–Ar ages**

632 A valid interpretation of illite isotopic ages in relation to deformation history is subject
633 to a solid mineralogical characterisation of samples. Particularly, information about the illite
634 crystallinity and illite polytype data are critical in assessing the illite crystallisation
635 temperature and a possible contamination of samples by metamorphic detrital muscovite
636 from the undeformed host rock. Illite crystallinity is commonly used to identify the
637 transitional anchimetamorphic zone between the diagenesis and epimetamorphic zone of low-
638 grade metamorphism. The boundary limit from diagenetic to anchimetamorpic conditions
639 has been reported to be at 0.52°2θ, whereas the anchizone-epizone boundary is set at
640 0.25°Δ2θ (Warr and Mählmann, 2015). Accordinly, KI values of <2 and 2-1 Julia Creek
641 illitic clays indicate diagenetic and anchizone metamorphic conditions. Since these illites
642 occur as a discrete phase (containing no expandable layers) and contain both $1M/M_1$ and $2M_1$
643 polytypes they indicate formation temperatures of about 200ºC and higher (cf., Hoffman and
644 Hower, 1979, Walker and Thompson, 1990). Although the $2M_1$ polytype has been known to
645 appear usually at temperatures higher than 250°C (Srodon and Eberl, 1984), its occurrence at
646 lower temperatures at about 200-250°C in co-existence with $1M/M_d$ has also been reported
647 (Walker and Thomson, 1990, Chen and Wang, 2007; Hejing et al., 2008). KI values show
648 considerable differences between samples from Julia Creek and Dobbyn areas (Fig. 10),

649 which clearly indicate different paleothermal conditions in different areas. <2 μm fractions of
650 Julia Creek fault gouge samples show similar KI values with insignificant changes with
651 depth, except a spike for the sample at 440.5 m (Fig. 10). Samples from Dobbyn 2 are
652 characterised by lower KI values and the dominance of $2M_1$ illite (Fig. 10, Table 1).

653 Our interpretation of the significance of K–Ar ages for fault gouge and matrix illite is
654 based on K–Ar age versus grain size and KI relationships (Fig. 7b and Fig. 11a, b, c). This
655 relationship can represent either an inclined or a parallel age spectrum. The parallel age
656 spectrum results from identical K–Ar ages of different size fractions within error,
657 representing internal consistency, which is regarded as geologically meaningful (e.g., Clauer
658 and Chaudhuri, 1995; Torgersen et al., 2014; Vialo et al., 2016). The inclined age spectrum
659 can arise from the presence of multiple illite generations, such as either an earlier authigenic
660 illite generation or inherited (detrital) components mixing with younger authigenic illites. The
661 slope of the spectrum is a function of the age difference between the two age end members.

662 Plotting KI values vs. K–Ar ages, fault gouge samples from Julia Creek 1 indicate
663 almost flat spectrums with identical (within error) or slightly decreasing ages between 1049 ±
664 25 and 1006 ± 23 Ma for most of the JC samples and at ~1100 Ma for sample JC-408) (Fig.
665 11a). These concordant K–Ar ages of samples with changing grain size (Fig 7b) and KI
666 values can those be considered as meaningful as indicating the timing of major deformation
667 events. Similarly, an age clustering around 1060 Ma of samples with changing grain sizes and
668 KI values is evident for matrix illites (Fig. 7c and Fig. 11c).

669 There are two different KI values vs K–Ar age populations of Dobbyn 2 fault gouges,
670 displayed by the shallow (above 441 m) and deeper (below 441 m) samples, which are
671 distinguished by higher and lower KI values, respectively. They show two parallel trends
672 with reasonably well negative correlations (Fig. 11a), which may be considered as mixing of
673 two possible end members. These may be represented by an earlier illite generation at ~1100

674 Ma (similar age as various size fractions of sample JC-408, see above) and a later illitization
675 or isotopic resetting at ~900 Ma. The correlations in Fig. 11b can also be interpreted as
676 indicating the effect of numerous and superimposed slip episodes during discrete faulting
677 events. A similar K–Ar age range but different extend for KI values of Dobbyn 2 fault gouges
678 indicate that different thermal conditions prevailed in the shallower and deeper parts (see the
679 discussion above for the illite crystallinity) occurred in the same time period. Although
680 decreasing K–Ar ages with increasing KI values of Dob samples could be due to decreasing
681 amount of detrital illite/muscovite with decreasing grain size, K–Ar ages for different size
682 fractions and KI values of sample Dob-389.6 (2-1, <2, 1-0.5, and 0.5.0.1μm), Dob-449.1 (2-
683 0.5, <2, 1-0.5,and <0.5μm), and Dob-476.6 (2-1and <2μm) are consistent within analytical
684 error. This, together with authigenic mineral textures of illites (Fig. 3), suggests that the
685 presence of detrital muscovite in <2 fractions is unlikely.

686 Lowest K–Ar ages associated with highest KI values indicate later recrystallisation of
687 illites in finer crystals or isotopic resetting of finer illites at relatively lower temperatures not
688 affecting the coarser size fractions. Thermally activated volume diffusion in clay minerals
689 leading to ^{40}Ar loss can cause decreasing K–Ar ages with decreasing grain sizes of clays
690 (e.g., Torgersen et al., 2014; Lerman, et al., 2007). The finest clay size fractions are more
691 susceptive to younger thermal events due to poor radiogenic argon retentivity because of
692 smaller diffusion radius and less crystallinity. Consequently, re-heating of earlier formed
693 finest particles during a later thermal event to a temperature high enough to enable ^{40}Ar
694 diffusion from the crystal structure could cause partial or complete resetting of the K–Ar
695 isotopic systematics (Clauer and Chaudhuri, 1999). Alternatively, the finest fraction
696 represents the last clay growth of newly crystallised tiny illite crystallites, which can occur
697 during fluid flow events related to tectonically active regimes (e.g., Zwingmann and
698 Mancktelow, 2004; Uysal et al., 2006). The size of authigenic clay minerals can be a function

699 of both the duration of crystal growth and the crystallisation temperature (Frey, 1987;
700 Cashman and Ferry, 1988). The ages of the finest grain size fractions therefore date either
701 the timing of the last, short-lived thermal and/or fluid flow events (c.f., Torgersen et al.,
702 2015) or cooling events after a prolonged burial and mineral growth, which took place in
703 Neoproterozoic latest.

704

705 **5.5. Significance for regional tectonics**

706 Northeast Australia lies on a cratonic margin that has had a complex crustal history
707 involving the successive development of several Proterozoic to Paleozoic orogenic systems
708 (Fig. 12). Age data from the faults defining the margins of the Millungera Basin is thus
709 important in revealing concealed major Proterozoic tectonic zones in Australia, which contain
710 energy and mineral resources (Korsch et al., 2011). The age data from the fault gouges
711 provide clear evidence for a late Mesoproterozoic minimum age for the Millungera Basin,
712 and are in accordance with the early-mid Mesoproterozoic maximum depositional age of the
713 Millungera Basin as constrained from zircon ages for Millungera Basin sandstones (Neumann
714 and Kositcin, 2011).

715 The fault gouge ages clustering at (~1115 ± 26 Ma, ~1070 ± 25 Ma, ~1040 ± 24 Ma,
716 ~1000 ± 23 Ma, and ~905 ± 21 Ma (Fig. 7) may be related to the regional extension and
717 associated major thermal event that occurred across Australia at 1120-900 Ma (e.g.,
718 Musgrave Orogeny and subsequent Giles Event), due to interactions between Australia and
719 other continents during assembly of the supercontinent Rodinia (De Vries et al., 2008; Li et
720 al., 2008; Evins et al., 2010). This Australia-wide tectono-thermal event that largely
721 developed along former (Mesoproterozoic) collision zones led to emplacement of widespread
722 dyke swarms, sills and associated granite plutons in the central and north Australia craton

723 largely in a time frame between ~1040 Ma and ~1090 Ma (Schmidt et al., 2006; Evins et al.,
724 2010; Aitken et al., 2013). The Musgrave Orogeny involving widespread emplacement of
725 granite and mafic–ultramafic bodies were recorded in central Australia at 1220 Ma and 1120
726 Ma (Evins et al., 2010; Kirkland et al., 2013). Major swarms of dolerite intrusions in the
727 North Australian Craton dated at 1116±12 Ma (Lakeview Dolerite, Tanaka and Idnurm,
728 1994) and associated hydrothermal events were recorded in the Mt. Isa Province (adjacent to
729 the study area, Fig. 1) (Uysal et al., 2004). The illite ages clustering around ~1100 Ma
730 coincide with the latest stage of the Musgrave Orogeny Fig. 7b, Fig. 12).

731 Another cycle of mafic intrusions in central Australia occurred during the extensional
732 Giles Event between ~1078 Ma and 1068 Ma (Evins et al., 2010; Aitken et al., 2013 and
733 references therein), which was followed by granite magmatism and accompanied felsic
734 volcanism between ~1050 Ma and ~1040 Ma (Evins et al., 2010 and references therein). The
735 latest phase of the Giles Event is represented by the felsic Smoke Hill Volcanics yielding a
736 age of 1026±26 Ma. The K–Ar ages clustering around ~1040 Ma of different illite size
737 fractions from the fault gouges and sandstones are consistent with the timing of the later stage
738 of the Giles event.

739 Orogenic events post-dating the Giles event are represented by mafic dykes and rare
740 pegmatites emplaced at about 1000 Ma (Evins et al., 2010). Further, a Rb–Sr age of 897 ± 9
741 Ma is reported for dolerite from the Stuart Dyke Swarm in the southern part of the Arunta
742 Block, Northern Territory (Black et al., 1980). The Rodinia supercontinent assembled
743 through worldwide orogenic events by 900 Ma. Stresses induced by the ca. 900 Ma event
744 probably caused reactivation of older orogens within Rodinia (Li et al., 2008). The Amadeus
745 Basin in north central Australia was initiated at ~900 Ma in the late Proterozoic by crustal
746 extension, probably in associations with mafic intrusions being correlated with the Stuart
747 Dyke Swarm (Korsch and Lindsay, 1989). Fault gouge K–Ar ages of ~900 – 950 Ma for

various size fractions from sample Dob-449.1 and finest fraction (<0.1 mm) from Dob-389.6 coincide with the timing of deformation associated with these early Neoproterozoic igneous and deformation events (Fig. 7b).

The dated faults of the Millungera Basin may be associated regionally with a series of fault systems bounding rift basins in the southern Georgina Basin. Those fault zones (e.g., Burke River Structural Belt, Pilgrim Fault Zone, Greene, 2010), which are in close proximity to and run parallel to the dated faults framing the Millungera Basin, occur extensively in the adjacent Mt Isa Inlier (Greene, 2010; Korsch et al., 2011). The Pilgrim Fault Zone was established a Mesoproterozoic structural boundary within the Mt. Isa Inlier (Greene, 2010). The southern Burke River Fault, just to the west of the Millungera Basin (Fig. 1), represents a rift-bounding normal fault, were reactivated and inverted to reverse faults during the mid-Paleozoic Alice Springs Orogeny (~400-350 Ma) (Greene, 2010). Similarly, samples from this study were taken from thrust faults at the margin of the Milungera Basin. However, the K–Ar, ^{40}Ar–^{39}Ar, and Rb–Sr ages of the fault gouge illites have been essentially preserved and no tectonic event after about 905 Ma has reset the isotopic systematics of these fault gouges (Fig. 12). This can be explained by the lack of significant fluid or heat flow events allowing recrystallisation or ^{40}Ar diffusion from illites. In conclusion, our geochronological age data constrain the timing of fault activity associated with the late Meseproterozoic and early Neoproterozoic emplacement of the intrusions and crustal regional extension in central-north Australia.

6. CONCLUSIONS

A new integrated study was conducted employing radiometric age dating (K–Ar, ^{40}Ar–^{39}Ar, and Rb–Sr) of illitic clay minerals from fault gouges and Neoproterozoic host sandstones bounding the recently discovered Millungera Basin in north-central Australia. Rb–Sr

772 isochron, ^{40}Ar–^{39}Ar total gas, and K–Ar ages are consistent indicating late Mesoproterozoic
773 and early Proterozoic episodes (~1115 ± 26 Ma, ~1070 ± 25 Ma, ~1040 ± 24 Ma, ~1000 ± 23
774 Ma, and ~905 ± 21 Ma) of active tectonics in north-central Australia. These faulting episodes
775 correspond to timing of regional extension and associated major thermal event that occurred
776 across Australia at 1120-900 Ma, due to interactions between Australia and other continents
777 during assembly of the supercontinent Rodinia. Sr isotope and trace element data indicate that
778 fault gouge illites precipitated from fluids that interacted with deep granitic basement
779 enriched in heat-producing elements. This study provides insight into the inscrutable time-
780 space distribution of Precambrian tectonic zones in central Australia, which are responsible
781 for the formation of a number of sedimentary basins with significant energy and mineral
782 resources. Investigating core samples with preserved isotopic signature of Proterozoic fault
783 rocks avoids the effect of surface weathering of old geological terranes.

784 **Acknowledgements**

785 Support for this research was provided by Queensland Geothermal Energy Centre of
786 Excellence (QGECE) funded by the Queensland State Government. Support by Hal Gurgenci
787 (former QGECE's director) is particularly acknowledged. The manuscript benefited from
788 comments by Tony Allan who is greatly appreciated. Espen Torgersen and Neil Mancktelow
789 are gratefully acknowledged for their very useful and constructive comments of an earlier
790 version of the paper, which helped significantly to improve the manuscript. Furthermore,
791 comprehensive reviews by Luca Aldega and Roelant van der Lelij and their constructive
792 comments and suggestions have greatly improved the manuscript. Michael Verrall is thanked
793 for his assistance for the SEM work. We thank Yue-xing Feng and Ai Duc Nguyen for their
794 help with analytical work and technical assistance to perform Rb–Sr and trace-element
795 analyses. We thank Turgay Demir for his assistance during sample preparation, and we
796 particularly acknowledge Chris Hall for his great help in undertaking the $^{40}Ar/^{39}Ar$ analysis at

797 the University of Michigan. We thank Norbert Clauer and Johannes Glodny for discussions
798 of the geochronological data. The Geological Survey of Queensland is particularly
799 acknowledged for providing access to core sampling.

800

801 **References**

802 Aitken A. R. A., Smithies R. H, M. C. Dentith, A. Joly, S. Evans and Howard H. M. (2013)
803 Magmatism-dominated intracontinental rifting in the Mesoproterozoic: The
804 Ngaanyatjarra Rift, central Australia. *Gondwana Res.*, 24, 886-901.

805 Algea, L. Viola, G., Casas-Sainz, A., Marcén, M., Román-Berdiel, van der Lelij. (2019)
806 Unraveling multiple thermo-tectonic events accom- modated by crustal-scale faults in
807 northern Iberia, Spain: Insights from K-Ar dating of clay gouges. *Tectonics*, **38**, 3629-
808 3651.

809 Árkai P. (1991) Chlorite crystallinity: an empirical approach and correlation with illite
810 crystallinity, coal rank and mineral facies as exemplified by Palaeozoic and Mesozoic
811 rocks of northeast Hungary. J. *Metamorph. Geol.* **9**, 723–734.

812 Babaahmadi, A., Uysal, I.T., Rosenbaum, G. (2019). Late Jurassic intraplate faulting in
813 eastern Australia: a link to subduction in eastern Gondwana and plate tectonic
814 reorganisation. *Gondwana Research*, **66**, 1-12.

815 Balsamo, F., Aldega, L., De Paola, N., Faoro, I., Storti, F. (2014). The signature and
816 mechanics of earthquake ruptures along shallow creeping faults in poorly lithified
817 sediments., *Geology*., **42**, 435-438.

818 Bense, F.A., Wemmer, K., Löbens, S. Siegesmund, S. (2014). Fault gouge analyses: K-Ar
819 illite dating, clay mineralogy and tectonic significance—a study from the Sierras
820 Pampeanas, Argentina. *International Journal of Earth Sciences*, **103**, 189-218.

821 Berthé D., Choukroune P. and Jégouzo, P. (1979) Orthogneiss, mylonite and non coaxial
822 deformation of granites: the example of the South Armorican Shear Zone. *J. Struct.*
823 *Geol*. **1**, 31-42.

824 Black L.P., Shaw R.D. and Offe, L.A. (1980) The age of the Stuart Dyke Swarm and its
825 bearing on the onset of late Precambrian sedimentation in central Australia. J. Soc.
826 Austr., 27, 151-155.

827 Boles A., van der Pluijm B., Mulch A., Mutlu H., Uysal I.T. and Warr, L. (2015) Hydrogen
828 and 40Ar/39Ar isotope evidence for multiple and protracted paleofluid flow events
829 within the long-lived North Anatolian Keirogen (Turkey). *Geochem. Geophy. Geosy*.
830 **16**, 1975-1987.

831 Bröcker, M., Baldwin, S., Arkudas, R. (2013). The geological significance of $^{40}Ar/^{39}Ar$ and
832 Rb–Sr white mica ages from Syros and Sifnos, Greece: a record of continuous
833 (re)crystallization during exhumation? *J. Metamorph. Geol*. **31**, 629–646.

834 Chen, T. and Wang, H.J. (2007). Determination of layer stacking microstructures and
835 intralayer transition of illite polytypes by high-resolution transmission electron
836 microscopy (HRTEM). *American Mineralogist*, **92**, 926-932.

837 Chester F.M., Friedman M. and Logan, J.M. (1985) Foliated cataclasites. *Tectonophysics*
838 **111**, 139-146.

839 Clauer, N. and Chaudhuri, S., 1995. Clays in Crustal Environments. Isotope Dating and
840 Tracing. Springer Verlag, Heidelberg, 359 p.

841 Clauer N., Chaudhuri S. Kralik S. and Bonnotcourtois C. (1993) Effects of experimental
842 leaching on Rb-Sr and K-Ar isotopic systems and REE contents of diagenetic illite,
843 *Chem. Geol.* **103**, 1-16.

844 Clauer N., Zwingmann H., Liewig N. and Wendling R. (2012) Comparative 40Ar/39Ar and
845 K-Ar dating of illite-type clay minerals: a tentative explanation for age identities and
846 differences. *Earth-Sci. Rev*. 115, 76–96.

847 Clauer, N. and Liewig, N. (2013) Episodic and simultaneous illitization in oil-bearing Brent
848 Group and Fulmar Formation sandstones from the northern and southern North Sea
849 based on illite K–Ar dating. *Am. Assoc. Pet. Geol. Bull*. **97**, 2149–2171.

850 Craw, D., Upton, P. and Mackenzie, D.J. (2009). Hydrothermal alteration styles in ancient
851 and modern orogenic gold deposits, New Zealand. *New Zealand Journal of Geology*
852 *and Geophysics*, **52**, 11-26.

853 Dalrymple G.B. and Lanphere, M.A. (1969) Potassium-argon dating. W.H. Freeman, San
854 Francisco, 258 p.

855 Davidson, J., Charlier, B., M.H., Perlroth, R. (2005). Mineral isochrons and isotopic
856 fingerprinting: Pitfalls and promises. *Geology*, **33**, 29–32.

857 de Vries S.T., Pryer L.L. and Fry N. (2008) Evolution of Neoarchaean and Proterozoic basins
858 of Australia. Precambr. Res., **166**, 39–53.

859 Delle Piane C., Clennell M.B., Keller J.V., Giwelli A. and Luzin, V. (2017) Carbonate hosted
860 fault rocks: A review of structural and microstructural characteristic with implications
861 for seismicity in the upper crust. *J. Struct. Geol*. **103**, 17-36.

862 Di Vincenzo G, Tonarini S, Lombardo B, Castelli D and Ottolini L. (2006) Comparison of
863 40Ar/39Ar and Rb-Sr data on phengites from the UHP Brossasco-Isasca unit (Dora
864 Maira Massif, Italy): implications for dating white Mica. *J. Petrol*. **47**, 1439–1465.

865 Duvall A.R., Clark M.K., van der Pluijm B.A. and Li C. (2011) Direct dating of Eocene
866 reverse faulting in northeastern Tibet using Ar-dating of fault clays and low-
867 temperature thermochronometry. *Earth Planet. Sci. Lett.* **304**, 520-526.

868 Eberl, D.D., Środoń, J., Kralik, M., Taylor, B.E, and Peterman, Z.E., 1990. Ostwald ripening
869 of clays and metamorphic minerals, Science 248, 474–477.

870 Eggins S.M., Woodhead J.D., Kinsley L.P.J., Mortimer G.E., Sylvester P., McCulloch M.T.,
871 Hergt J.M. and Handler M.R. (1997) A simple method for the precise determination
872 of >=40 trace elements in geological samples by ICPMS using enriched isotope
873 internal standardization. *Chem. Geol.* **134**, 311-326.

874 Eichhubl, P., Davatzes, N.C., and Becker, S.P. (2010). Structural and diagenetic control of
875 fluid migration and cementation along the Moab fault, Utah. AAPG Bulletin, 93, 653-
876 681.

877 Elminen T., Zwingman, H. and Kaakinen A. (2018) Timing of brittle deformation and
878 sedimentation within the Savio tunnel site, Southern Finland – Implication for
879 sediment sources in Fennoscandia. – Precambrian Research, 304, 110-124,
880 doi.org/10.1016/j.precamres.2017.10.014

881 Evins P.M., Smithies R.H., Howard H.M., Kirkland C.L., Wingate M.T.D. and Bodorkos S.
882 (2010) Redefining the Giles Event within the setting of the 1120–1020 Ma
883 Ngaanyatjarra Rift, west Musgrave Province, Central Australia. *Geological Survey of*
884 *Western Australia, Record* 2010/6, 36p.

885 Faulkner, D. R., Jackson, C. A. L., Lunn, R. J., Schlische, R. W., Shipton, Z. K., Wibberley,
886 C. A. J., and Withjack, M. O. (2010). A review of recent developments concerning the
887 structure, mechanics and fluid flow properties of fault zones. Journal of Structural
888 Geology 32, 1557–1575.

889 Faulkner S.P., Maxwell M., O'connor L.K., Sargent S.N., and Talebi B. (2012) Coastal
890 Geothermal Energy Initiative GSQ Julia Creek 1: well completion report and heat
891 flow modelling results. *Queensland Geological Record* 2012/05.

892 Fedo, C.M., Nesbitt, H.W., Young and G.M. (1995). Unraveling the effects of potassium
893 metasomatism in sedimentary rocks and paleosols, with implications for
894 paleoweathering conditions and provenance. *Geology*, **23**, 21–924.

895 Frey, M. (1987). Very-low-grade metamorphism of clastic sedimentary rocks. In: Low
896 temperature Metamorphism, M. Frey, editor. Blackie and Son, Glasgow. 351 pp.

897 Ferry, J.M. and Dipple, G.M. (1991). Fluid flow, mineral reactions, and metasomatism.
898 *Geology*, **19**, 211-214.

899 Fitzell M.J., Maxwell M., O'connor L.K., Sargent S.N. and Talebi B. (2012) Coastal
900 Geothermal Energy Initiative, GSQ Dobbyn 2 Well completion report and heat flow
901 modelling results. *Queensland Geological Record* 2012/04.

902 Golding, S.D., Uysal, I.T., Bolhar, R., Boreham, C.J. Dawson, G.K.W., Baublys, K.A., and
903 Esterle, J.S. (2013). Carbon dioxide-rich coals of the Oaky Creek area, central Bowen
904 Basin: a natural analogue for carbon sequestration in coal systems. *Australian Journal*
905 *of Earth Sciences*, **60**, 125-140.

906 Grathoff G.H. and Moore D.M. (1996) Illite polytype quantification using Wildfire©
907 calculated X-ray diffraction patterns. *Clay. Clay Miner.* (44) 835–842.

908 Greene, D.C. (2010) Neoproterozoic rifting in the southern Georgina Basin, central Australia:
909 Implications for reconstructing Australia in Rodinia. *Tectonics* **29**, TC5010,
910 doi:10.1029/2009TC002543.

911 Hall C. M. (2014) Direct measurement of recoil effects on ^{39}Ar-^{40}Ar standards. *Geol. Soc.*
912 *London Spec. Publ*., **378**, 53-62.

913 Hall C. M., Higueras P. L., Kesler S. E., Lunar R., Dong H. and Halliday A. N. (1997) Dating
914 of alteration episodes related to mercury mineralisation in the Almade´n district,
915 Spain. *Earth Planet. Sci. Lett*. **148**, 287–298.

916 Hejing, W., Rahn, M., Xiaofeng, T., Nan, Z., Tingjing, X. (2008). Diagenesis and
917 metamorphism of Triassic Fflysch along profile Zoige-Lushan, Northwest Sichuan,
918 China. *Acta Geologica Sinica*. **82**, 917-926.

919 Hess, J.C and Lippolt, H.J. (1994). Compilation of K-Ar measurements on HD-B1 standard
920 biotite. in : Odin G.S. (1994) : Phanerozoic time scale, Bull. Lias. Inform., IUGS
921 subcom. Geochronol., 12, Paris p. 19-23.

922 Hetzel, R., Zwingmann, H., Mulch, A., Gessner, K., Akal, C., Hampel, A., Güngör, T.,
923 Petschick, R., Mikes, T. and Wedin, F. (2013) Spatiotemporal evolution of brittle
924 normal faulting and fluid infiltration in detachment fault systems: a case study from
925 the Menderes Massif, western Turkey. Tectonics 32, 1–13.

926 Hoffman, J. and Hower, J. (1979) Clay mineral assemblages as low grade metamorphic
927 geothermometers: Application to the thrust faulted disturbed belt of Montana. In:
928 Scholle, P.A. and Schluger, P.S., editors. Aspects of Diagenesis, SEPM Spec. Publ.,
929 26, 55-79.

930 Işik V. and Uysal I.T., Caglayan A. and Seyitoglu G. (2014) The evolution of intra-plate fault
931 systems in central Turkey: structural evidence and Ar–Ar and Rb–Sr age constraints
932 for the Savcili Fault Zone. *Tectonics* **33**, 1875–1899.

933 Ji J. and Browne P.R.L. (2000) Relationship between illite crystallinity and temperature in
934 active geothermal systems of New Zealand: Clay. Clay Miner. **48**, 139–144.

935 Kelley S. (2002) Excess argon in K–Ar and Ar–Ar geochronology. *Chem. Geol.* **188**, 1 – 22

936 Kirkland, C.L., Smithies, R.H., Woodhouse, A.J., Howard, H.M., Wingate, M.T.D.,
937 Belousova, E.A., Cliff, J.B., Murphy, R.C., Spaggiari, C.V. (2013). Constraints and
938 deception in the isotopic record; the crustal evolution of the west Musgrave
939 Province, central Australia. *Gondwana Research*, **23**, 759–781.

940 Korsch R.J., Lindsay, J.F. (1989). Relationships between deformation and basin evolution in
941 the intracratonic Amadeus Basin, central Australia. *Tectonophysics*, **158**, 5-22.

942 Korsch R.J., Struckmeyer H.I.M. Kirkby L.J., Hutton L.J., Carr L.K., Hoffmann K.,
943 Chopping R., Roy I.G., Fitzell M., Totterdell J.M., Nicoll M.G. andTalabi B. (2011)
944 Energy potential of the Millungera Basin: a newly discovered basin in north
945 Queensland. *The APPEA Journal* **51**, 295-332.

946 Korsch R. J., Huston D. L., Henderson R. A., Blewett R. S., Withnall I. W., Fergusson C. L.,
947 Collins W. J., Saygin E., Kositcin N., Meixner A. J., Chopping R., Henson P. A.,
948 Champion D. C., Hutton L. J., Wormald R., Holzschuh J. and Costelloe R. D.
949 (2012) Crustal architecture and geodynamics of North Queensland, Australia:
950 insights from deep seismic reflection profiling. *Tectonophysics* **572-573**, 76-99.

951 Laurich B., Urai J.L., Desbois G., Vollmer C. and Nussbaum C. (2014). Microstructural
952 evolution of an incipient fault zone in Opalinus Clay: Insights from an optical and
953 electron microscopic study of ion-beam polished samples from the Main Fault in the
954 Mt-Terri Underground Research Laboratory. *J. Struct. Geol*. **67**, 107-128.

955 Lee J. I. and Lee Y. I. (2001). Kübler illite crystallinity index of the Cretaceous Gyeongsang
956 Basin, Korea: southeastern Korea: Implications for basin evolution. *Clays and Clay*
957 *Minerals* **49**, 36–43.

958 Li H.-C., Ku T.-L., You C.-F., Cheng H., Lawrance Edwards R., Ma Z.-B., Tsai A.-S. and Li
959 M.-D. (2005) 87Sr/86Sr and Sr/Ca in speleothems for paleoclimate reconstruction
960 in Central China between 70 and 280 kyr ago. Geochim. Cosmochim. Acta 69,
961 3933–3947.

962 Li, Z. X., X. H. Li, P. D. Kinny, and J. Wang (1999), The breakup of Rodinia: Did it start
963 with a mantle plume beneath south China? *Earth Planet. Sci. Lett*., **173**, 171–181

964 Li Z. X.; Bogdanova S. V., Collins A. S., Davidson A., De Waele B., Ernst R. E., Fitzsimons
965 I. C. W., Fuck R. A., Gladkochub D. P., Jacobs J., Karlstrom K. E., Lul S., Natapov
966 L. M., Pease V., Pisarevsky S. A., Thrane K., Vernikovsky V. (2008) Assembly,
967 configuration, and break-up history of Rodinia: A synthesis. *Precambr. Res*.
968 **160**,179–210.

969 Lin A. (1999) S–C cataclasite in granitic rock. *Tectonophysics* **304**, 257-273.

970 Lonker S.W. and Gerald J.D.F. (1990) Formation of coexisting 1M and $2M_1$ polytypes in
971 illite from an active hydrothermal system. *Amer. Miner*. **75**, 1282-1289.

972 Ludwig K.R. (2012) User'sManual for Isoplot/Ex: a Geochronological Toolkit for Mi-crosoft
973 Excel, 70pp.

974 Lupi, M., S. Geiger, and C. M. Graham (2010), Hydrothermal fluid flow within a tectonically
975 active rift-ridge transform junction: Tjörnes Fracture Zone, Iceland, *J. Geophys.*
976 *Res.*, **115**, B05104, doi:10.1029/2009JB006640.

977 Maffucci, R. Corrado, S., Aldega, L., Bigi, S., Chiodi, A., Di Paolo, L., Giordano, G. and
978 Invernizzi, C. (2016). Cap rock efficiency of geothermal systems in fold-and-thrust
979 belts: Evidence from paleo-thermal and structural analyses in Rosario de La
980 Frontera geothermal area (NW Argentina). *Journal of Volcanology and*
981 *Geothermal Research*, **328**, 84-95.

982 Mancktelow N., Zwingmann H., Campani M., Fugenschuh B., Mulch A. (2015) Timing and
983 conditions of brittle faulting on the Silltal-Brenner Fault Zone, Eastern Alps
984 (Austria). *Swiss J Geosci* **108**, 305–326.Mancktelow, N., Zwingmann, H. and
985 Mulch, A. (2016) Dating of fault gouge from the Naxos detachment (Cyclades,
986 Greece). Tectonics 35 (10), 2334–2344.

McDougall, I., Roksandic, Z. (1974). Total fusion 40Ar/39Ar ages using HIFAR reactor. Journal of the Geological Society of Australia, 21, 81-89.

Merrriman R. J. and Frey M. (1999) Patterns of very low-grade metamorphism in metapelitic rocks. In *Low Grade Metamorphism* (eds. M. Frey and D. Robinson). Blackwell Science, Cambridge. pp. 61–107.

Merrriman R. J. and Peacor D.R. (1999) Very low-grade metapelites: mineralogy, microfabrics and measuring reaction progress. In *Low Grade Metamorphism* (eds. M. Frey and D. Robinson). Blackwell Science, Cambridge. pp. 10–60.

Michalski, J.R., Reynolds, S.J., Niles, P.B., Sharp, T.G. and Christensen, P.R. (2007). Alteration mineralogy in detachment zones: Insights from Swansea, Arizona. Geosphere, 3, 84–198.

Middleton A.W., Uysal I.T., Bryan S.E., Hall C.M. and Golding S.D (2014) Integrating ^{40}Ar–^{39}Ar, ^{87}Rb–^{87}Sr and ^{147}Sm–^{143}Nd geochronology of authigenic illite to evaluate tectonic reactivation in an intraplate setting, central Australia. *Geochim. Cosmochim. Acta.* **134**, 155-174.

Mutlu H., Uysal I. T., Altunel, E., Karabacak V., Feng Y., Zhao J.-x. and Atalay O. (2010) Rb–Sr systematics of fault gouges from the North Anatolian Fault Zone (Turkey), J. Struct. Geol. **32**, 216-221.

Myers, J.S., Shaw, R.D. and Tyler, I.M. (1996). Tectonic evolution of Proterozoic Australia, *Tectonics*, **15**, 1431–1446.

Neumann, N.L. and Kositcin, N. (2011). New SHRIMP U-Pb zircon ages from north Queensland, 2007–2010. *Geoscience Australia, Record*, **2011/38**, 82 p.

1009 Nicchio M.A., Nogueira F.C., Balsamo F., Souza J.A., Carvalho B.R. and Bezerra F.H.
1010 (2018) Development of cataclastic foliation in deformation bands in feldspar-rich
1011 conglomerates of the Rio do Peixe Basin, NE Brazil. *J. Struct. Geol*. **107**, 132-141.

1012 O'Dea, M. G., Lister, G. S., MacCready, T., Betts, P. G., Oliver, N. H. S., Pound, K. S.,
1013 Huang, W. and Valenta, R. K. 1997. Geodynamic evolution of the Proterozoic
1014 Mount Isa terrain. In Orogeny Through Time, Edited by: Burg, J. P. and Ford, M.
1015 Vol. 121, 99–122. Geological Society of London Special Publication.

1016 Odin G.S. and 35 collaborators (1982). Interlaboratory standards for dating purposes. in:
1017 Odin, G.S. (editor) Numerical Dating in Stratigraphy. Part 1. John Wiley & Sons,
1018 Chichester, 123-148.

1019 Ohr M., Halliday A.N. and Peacor D.R. (1994) Mobility and fractionation of rare earth
1020 elements in argillaceous sediments: Implications for dating diagenesis and low-
1021 grade metamorphism. *Geochim. Cosmochim. Acta.* **58**, 289-312.

1022 Parry, W. T., Hedderly-Smith, D., And Bruhn, R. L. (1991), Fluid Inclusions and
1023 Hydrothermal Alteration on the Dixie Valley Fault, Nevada. *J. Geophys. Res*., **96**,
1024 19,733-19,748.

1025 Rosenbaum G., Uysal I.T. and Babaahmadi A. (2015) The Red Rock Fault Zone (northeast
1026 New South Wales): Kinematics, timing of deformation and relationships to the New
1027 England oroclines. Aust. J. Earth. Sci. **62**, 409-423.

1028 Rossetti, F., Aldega, L., Tecce, F., Balsamo, F. (2011) Fluid flow within the damage zone of
1029 the Boccheggiano extensional fault (Larderello–Travale geothermal field, central
1030 Italy): structures, alteration and implications for hydrothermal mineralization in
1031 extensional settings. *Geological Magazine* **148**, 558–579.

1032 Rowe C.D., Kirkpatrick J.D. and Brodsky E.E. (2012) Fault rock injections record paleo-
1033 earthquakes. *Earth Planet. Sci. Lett*. **335**, 154-166.

1034 Rutter E.H., Maddock R.H., Hall S.H. and White S.H. (1986) Comparative microstructures of
1035 natural and experimentally produced clay-bearing fault gouges. Pure Appl.
1036 Geophys. **124**, 3-30.

1037 Schmid S. M. and M. R. Handy (1991) Towards a genetic classification of fault rocks:
1038 Geological usage and tectonophysical implications. In Controversies in Modern
1039 Geology: Evolution of Geological Theories in Sedimentology, Earth History and
1040 Tectonics (eds. D. W. Mueller, J. A. McKenzie and H. Weissert). Academic, San
1041 Diego, Calif. pp. 339–361.

1042 Schmidt P.W., Williams G.E., Camacho A. and Lee, J.K.W. (2006) Assembly of Proterozoic
1043 Australia: implications of a revised pole for the ~1070 Ma Alcurra Dyke Swarm,
1044 central Australia. *Geophys. J. Int*. **167**, 626–634.

1045 Schneider, J., Haack, U., Stedingk, K. (2003). Rb-Sr dating of epithermal vein mineralization
1046 stages in the eastern Harz Mountains (Germany) by paleomixing lines. *Geochimica*
1047 *et Cosmochimica Acta*, **67**, 1803-1819.

1048 Scott, D.L., Rawlings, D.J., Page, R.W., Tarlowski, C.Z., Idnurm, M., Jackson, M.J. and
1049 Southgate, P.N., (2000) Basement framework and geodynamic evolution of the
1050 Palaeoproterzoic superbasins of north- central Australia: an integrated review of
1051 geochemical, geochronological and geophysical data. Australian Journal of Earth
1052 Sciences, 47, 341-380.

1053 Sharp Z. D. (1990) A laser-based microanalytical method for the in situ determination of
1054 oxygen isotope ratios of silicates and oxides: *Geochim. Cosmochim. Acta.* **54**, 1353-
1055 1357.

1056 Sibson R. H. (1977) Fault rocks and fault mechanisms. *J. Geol. Soc. Lond.* **133**, 191–213.

1057 Sibson R. H. (1987) Earthquake rupturing as a hydrothermal mineralising agent. *Geology* **15**,
1058 701-704.

1059 Sibson R.H. (1989) Earthquake faulting as a structural process. Journal of Structural *Geology*
1060 **11**, 1-14.

1061 Smeraglia, L., Aldega, L. Billi, A., Carminati, E., Doglioni, C. (2016). Phyllosilicate
1062 injection along extensional carbonate-hosted faults and implications for co-seismic
1063 slip propagation: case studies from the central Apennines, Italy. *J. Struct. Geol*., **93**,
1064 29-50.

1065 Solum J.G. van der Pluijm, B.A. and Peacor D.R. (2005) Neocrystallization, fabrics and age
1066 of clay minerals from an exposure of the Moab Fault, Utah. J. Struct. Geol. **27**,
1067 1563-1576.

1068 Srodon J. and Eberl, D.D. 1984. Illite. In *Micas*. (ed. S.W. Bailey). Reviews in mineralogy
1069 13, Mineralogical Society of America. pp. 495-544.

1070 Steiger R.H. and Jäger E. (1977) Subcommission on geochronology: convention on the use
1071 of decay constants in geochronology and cosmochronology. *Earth. Planet. Sci. Lett*.
1072 **36**, 359–362.

1073 Tanaka H. and Idnurm. M (1994). Palaeomagnetism of Proterozoic mafic intrusions and host
1074 rocks of the Mount Isa Inlier, Australia: revisited. *Precambr. Res*. **69**, 241-258.

1075 Taylor S.R. and McLennan S.M. (1985) *The Continental Crust: Its Composition and*
1076 *Evolution*. Blackwell, 312.

1077 Taylor H. P. (1997) Oxygen and hydrogen isotope relationships in hydrothermal mineral
1078 deposits. In *Geochemistry of hydrothermal ore deposits.* (ed. H. L. Barnes). John
1079 Wiley, New York. pp. 229–288.

1080 Torgersen E., Viola G., Zwingmann H. and Harris C. (2014) Structural and temporal
1081 evolution of a reactivated brittle-ductile fault—Part II: timing of fault initiation and
1082 reactivation by K-Ar dating of synkinematic illite/muscovite. *Earth. Planet. Sci.*
1083 *Lett.* **407**, 221–233

1084 Ujiie K., Yamaguchi A., Kimura G. and Toh, S. (2007) Fluidization of granular material in a
1085 subduction thrust at seismogenic depths. *Earth. Planet. Sci. Lett.*, **259**, 307-318.

1086 Uysal I.T. and Golding S.D. (2003) Rare earth element fractionation in authigenic illite-
1087 smectite from Late Permian clastic rocks, Bowen Basin, Australia: implications for
1088 physico-chemical environments of fluids during illitization. *Chem. Geol*. **193**, 167-
1089 179.

1090 Uysal I.T., Glikson M., Golding S.D. and Southgate P.N. (2004) Hydrothermal control on
1091 organic matter alteration and illite precipitation, Mt Isa Basin, Australia. *Geofluids*
1092 **4**, 131-142.

1093 Uysal I.T., Mory A.Y., Golding S.D., Bolhar R. and Collerson K.D. (2005). Clay
1094 mineralogical, geochemical and isotopic tracing of the evolution of the Woodleigh
1095 impact structure, Southern Carnarvon Basin, Western Australia. Contrib. Mineral.
1096 Petrol. **149**, 576-590.

1097 Uysal I. T., Mutlu M, Altunel A., Karabacak V. and Golding S. D. (2006) Clay mineralogical
1098 and isotopic (K–Ar, δO-18, δD) constraints on the evolution of the North Anatolian
1099 fault zone, Turkey. *Earth. Planet. Sci. Lett.* **243**, 181–194.

1100 Uysal I.T., Golding S.D, Bolhar R., Zhao J-X., Feng Y., Greig A. and Baublys K. (2011) CO_2
1101 degassing and trapping during hydrothermal cycles related to Gondwana rifting in
1102 eastern Australia. *Geochim. Cosmochim. Acta.* **75**, 5444–5466.

1103 Vance D, Ayres M, Kelley SP and Harris NBW (1998) The thermal response of a
1104 metamorphic belt to extension: constraints from laser Ar data on metamorphic
1105 micas. *Earth. Planet. Sci. Lett.* **162**,153-164

1106 van der Pluijm B.A., Hall C.M., Vrolijk P.J., Pevear D.R. and Covey M.C. (2001) The dating
1107 of shallow faults in the Earth's crust. *Nature* **412**: 172-175.

1108 Verdel C., van der Pluijm,B. A. and Niemi N. (2012) Variation of illite/muscovite 40Ar/39Ar
1109 spectra during progressive low-grade metamorphism: an example from the US
1110 Cordillera. *Contrib. Mineral. Petr*. **164**, 521–536.

1111 Villa, I.M. De Bièvre, P.; Holden, N.E.; Renne, P.R. (2015). IUPAC-IUGS recommendation
1112 on the half life of 87Rb. Geochimica et cosmochimica acta, 164, 382-385.

1113 Viola G, Zwingmann, H., Mattila, J., Käpyaho, 2013. K-Ar illite age constraints on the
1114 Proterozoic formation and reactivation history of a brittle fault in Fennoscandia. Terra
1115 Nova. **25**, 236-244.

1116 Viola G., Scheiber T., Fredin O., Zwingmann H., Margreth A., Knies J. (2016)
1117 Deconvoluting complex structural histories archived in brittle fault zones. Nat.
1118 Commun. **7**, 13448, 1-10.

1119 Vrolijk P. and van der Pluijm B.A. (1999) Clay gouge. *J. Struct. Geol*. **21**, 1039-1048.

1120 Walker, J.R. and Thompson, G.R. (1990). Structural variations in chlorite and illite in a
1121 diagenetic sequence from the Imperial Valley, Caslifornia. *Clays and Clay*
1122 *Minerals*. **38**, 315-321.

1123 Walter, M.R., Veever, J.J., Calver, C.R., Grey, K. (1995). Neoproterozoic stratigraphy oft he
1124 Centralian Superbasin, Australia. *Precambrian Research*, **73**, 173-195.

1125 Warr L.N. and Nieto, F. (1998) Interlaboratory standardization and calibration of clay
1126 mineral crystallinity and crystallite size data. J. Metamorph. Geol. **12**, 141–152

1127 Warr L. N. and Mählmann R.F. (2015) Recommendations for Kübler Index standardization.
1128 *Clay Miner*. **50**, 283–286.

1129 Wendt, I. (1993). Isochron or mixing line? *Chemical geology*, **104**, 301-305.

1130 Withnall, IW., Hutton, LJ., Armit, RJ., Betts, PG., Blewett, RS., Champion, DC., and Jell,
1131 PA. (2013). North Australian Craton. In P. A. Jell (Ed.), Geology of Queensland
1132 (pp. 23-112). Brisbane Qld Australia: Geological Survey of Queensland.

1133 Yamasaki S., Zwingmann H., Yamada K., Tagami T. & Umeda K. (2013) Constraining
1134 timing of brittle deformation and faulting in the Toki granite, central Japan.
1135 Chemical Geology, 351, 168–174.

1136 Zwingmann, H. and Mancktelow, N. (2004) Timing of Alpine fault gouges. Earth Planet. Sci.
1137 Lett. 223 (2–4), 415–425.

1138 Zwingmann H., Mancktelow N., Antognini M., Lucchini R. (2010) Dating of shallow faults
1139 —new constraints from the Alp Transit tunnel site (Switzerland). *Geology* **38**, 487–
1140 490.

1141

1142 **Figure captions**

1143 **Figure 1.** (a) Simplified map of north-central Australia showing the interpreted subsurface
1144 distribution of the Millungera Basin. The surface distribution of Cenozoic and Mesozoic
1145 sediments and the locations of the Proterozoic–Ordovician Basins are also shown (modified
1146 from Korsch et al., 2011). (b) Interpreted migrated seismic section for part of seismic line
1147 07GA-IG1 across the Millungera Basin, showing interpreted structures and sequence
1148 boundaries below the base Carpentaria unconformity (from Korsch et al., 2011).

1149 **Figure 2.** Photos of sampled cores showing fault gouges investigated in this study. Foliated
1150 and veined clay-rich fault gouges with light grey – green colour distinctive from adjacent
1151 brown hematite-rich sandstone host rock (a-e). Fault gouge veins are characterized by an
1152 ultrafine-to fine-grained matrix and angular to sub-angular fragments of host sandstone of
1153 various sizes, ranging from submicron to centimetres (b). Ultracataclastic veins are common,
1154 which are observed as simple veins, complex lenses, and networks (c-d). Foliated fault gouge
1155 zone with alternating red hematite-rich and grey – green layers (e). Slickenside structure is a
1156 commonly seen at the sharp contact between the clay-rich fault gouge layers and the host
1157 rock (f-g).

1158 **Figure 3.** Thin section photomicrographs (a-b) and SEM images (c-f) illustrating fault gouge
1159 illites from the Millungera Basis. (a) Illite plates (white) occur in voids within detrital quartz
1160 grains and as pore-filling clay together with chlorite between detrital grains. Note green –
1161 yellow chlorite shown by red arrow. (b) Alteration of detrital muscovite in illite. Note illite
1162 plates at the ends of the mica filling pores. (c) SEM image of sample Dob-441. Note the large
1163 detrital mica grain (>2 μm) with diffuse-blurred and irregular edges (the white material on
1164 the right-hand site), while authigenic illites occur in smaller crystals (<2 μm) with straight
1165 edges. SEM image of upper anchi-and epizone sample Dob-476.6. Note rounded smaller

1166 crystals (arrows), which occur partly as a constituent of larger illite plates (dashed arrows).
1167 (e-f) SEM images of samples JC-408 and JC-360.7, respectively. Note euhedral (hexagonal)
1168 and anhedral crystal plates with sharp and straight edges of these JC samples, which occur in
1169 smaller crystal size in comparison to the Dob samples. Smaller crystal size is consistent with
1170 higher KI values of JC samples (see Table 1).

1171 Figure 4. Microstructures of a faulted sample from Julia Creek 1 well (depth 360 m),
1172 petrographic thin section is cut parallel to the inferred shear direction. A) Whole thin section
1173 image collected using an optical microscope in plane polarised light showing composite S-C
1174 foliation (red dashed lines illustrate the orientation of the S plane. B) Optical microscope
1175 image in cross polarised light showing phyllosilicate enriched C-planes and the oblique S-
1176 foliation. C) Optical microscope image in cross polarised light showing alignment of opaque
1177 insoluble minerals along the S-plane (highlighted by the red arrows) indicative of pressure
1178 solution. D and E) Scanning electron microscope images of the deformed rock showing
1179 corroded boundaries in detrital quartz (Qtz) highlighted by the red arrows, authigenic
1180 kaolinite and illite (Kln; Ill) and detrital muscovite (Ms) aligned along the C plane.

1181 **Figure 5:** Faulted sample from Dobbyn 2 well (depth 441 m). A) Hand specimen showing
1182 green-beige slickenside surface with striations due to frictional movement along the surface.
1183 B) Polished face of the hand specimen cut parallel to the shear direction as inferred from the
1184 striation direction shown in A). C) Whole thin section image collected using an optical
1185 microscope in planes polarised light. The position of the thin section with respect to the hand
1186 specimen is shown by the red rectangle in B); yellow dashed line bound different
1187 microstructural domains of the fault rock defined as i) foliated cataclasite and ii) cataclasite.
1188 White boxes indicate the location of the following images. D) Optical microscope image in
1189 plane polarised light showing the slickenside surface (bound by the yellow dashed line) of the
1190 samples being composed of iso-aligned phyllosilicates. Also shown is a hematite rich

injection vein. E) Scanning electron microscope image of the foliated cataclasite portion of the samples and the characteristic S-C-C' texture (see text for details). White dashed line highlights the orientation of the S-planes. F) Optical microscope image in plane polarised light showing a slip surface (bound by the yellow dashed line) at the boundary between the foliated and non-foliated cataclasite domains. G) Optical microscope image in plane polarised light showing a network of hematite filled intra-crystalline micro-fractures in the cataclasite domain of the fault rock, mainly composed of quartz (white grains) and pore filling clays.

Figure 6. Ar–Ar dating results and argon release diagrams for illites from the fault gouges of <2 μm size fraction, for sanple Dob-476.6 (a), Dob-441 (b), JC-408, and JC-360.7 (c). Note consistent Ar–Ar total gas ages except for sample Dob-476.6.

Figure 7. A) Histogram for K–Ar and Ar–Ar ages and probability distribution of ages for fault gouge illites. Curves show relative probabilities calculated using Isoplot 7 for Excel (Ludwig, 2012). B) K–Ar and Ar–Ar dates (no error bars due to small errors) for different size fractions of fault gouges and C) matrix illites from host rocks and their interpretation in relation to tectonic history.

Figure 8. A) Rb-Sr data of the different size fractions and the untreated, leachate and residue separates of each size fractions from sample. Parallel linear relationships correspond to similar isochron age, but with different initial $^{87}Sr/^{86}Sr$ values. B) Rb-Sr plot for untreated and residues of <2 μm fractions from most Julia Creek 1 samples. C)Well-defined isochron for Julia Creek 1 samples after omitting two untreated aliquots D) Rb–Sr isochron diagrams for an assemblage of Dobbyn 2 samples (including JC-360.7B <0.5 μm) and E) another group of Dobbyn 2 samples with a younger age.

Figure 9. REE patterns of the fault gouge illites. Note that the illites are substantially enriched in light REE (LREE) relative to PAAS.

1215 Figure 10. KI values versus present depth from boreholes Jolokia 1 and Dobbyn 2.

1216 Figure 11. Correlations between K–Ar ages and KI values for fault gouge illites for samples
1217 from Dobbyn 2 (A), Julia Creek 1 (B) and matrix illites from sandstone host rocks (C) (>2μm
1218 fractions were not included). Analytical errors of K–Ar ages were disregarded for the
1219 regression lines. Exponential trends were obtained for the best fit of the regression lines for
1220 Dobbyn 2 samples (A). Note the flat trends that are obvious for Julia Creek 1 samples for
1221 fault gouges (B) and matrix illites (C).

1222 Figure 12. Summary of the geological history of the Millungera basin region and isotopic age
1223 clusters of the illites.

1224

Table 1. Clay mineralogy and age data of fault gouges and host rocks from Julia Creek 1 (JC) and Dobbyn 2 (Dob).

Sample & size fraction	Clay mineralogy	KI (Δ2θ)	AI (Δ2θ)	Very-low-grade metamorphic zone	$2M_1$ %	1M %	$1M_d$ %	Rb–Sr isochron age (Ma) (2σ)	Ar–Ar total gas age (Ma) (1σ)	K–Ar age (Ma) (2σ)	K_2O (%)	$^{40}Ar_{rad}$ (%)	$^{40}Ar_{rad}$ (10^{-10}mol/g)
Fault gouge													
JC-321 <2mm	illite	0.59		Diagenesis									
JC-326.1 <2μm	illite	0.69		Diagenesis									
JC-343.3 <2μm	illite, kaol., chl.	0.63		Diagenesis	68	14	18			1044.0 ± 24.4	7.10	99.3	174.1
JC-343.3 0.5-0.1μm	illite, kaol., chl.	0.79		Diagenesis						1039.2 ± 24.0	6.86	99.7	167.2
JC-343.3 <0.1μm	illite	0.92		Diagenesis						1025.3 ± 23.7	6.33	99.6	151.6
JC-360.7 <2μm	illite, kaol., chl.	0.63		Diagenesis	66	18	16	1023 ± 12	1038.1 ± 2.9	1014.9 ± 23.7	7.61	99.3	179.8
JC-360.7 2-1μm	illite, kaol., chl.	0.65		Diagenesis	58	22	20			1038.9 ± 24.0	7.49	99.4	182.5
JC-360.7 <1μm	illite, kaol., chl.	0.73		Diagenesis						1041.1 ± 24.1	7.49	99.5	183.0
JC-360.7 <0.5μm	illite	0.75		Diagenesis				1033 ± 25		1005.5 ± 23.1	7.65	99.6	178.6
JC-387.8 <2μm	illite, kaol., chl.	0.57		Diagenesis				1023 ± 12					
JC-408 >2μm	illite, kaol., chl.	0.42		Upper anchizone						1243.2 ± 29.1	7.64	99.7	237.1
JC-408 2-1μm	illite, kaol., chl.	0.63		Diagenesis	63	14	23			1118.7 ± 25.9	7.94	99.6	213.4
JC-408 <2μm	illite, kaol., chl.	0.60		Diagenesis	64	17	19		1040.0 ± 2.3	1115.8 ± 26.1	7.88	99.5	211.1
JC-408 <1μm	illite, kaol., chl.	0.70		Diagenesis	64	15	22			1118.2 ± 25.9	7.81	96.6	209.8
JC-408 <0.5μm	illite	0.82		Diagenesis						1104.0 ± 25.4	7.82	99.7	206.5
JC-430.4 <2μm	illite, kaol., chl.	0.51		Lower anchizone									
JC-440.5 <2μm	illite, kaol., chl.	0.44		Lower anchizone	58	24	18	1023 ± 12		1048.9 ± 24.5	6.60	99.4	176.3
JC-440.5 0.5-0.1μm	illite, kaol., chl.	0.84		Diagenesis						1020.3 ± 23 .6	7.41	99.8	168.8
JC-440.5 <0.1μm	illite	1.01		Diagenesis						1017.6 ± 23 .5	7.12	99.8	168.8
JC-473-A <2μm	illite, chl.	0.51	0.35	Lower anchizone									
JC-473-B <2μm	illite, chl.	0.47		Lower anchizone									
JC-483.2 <2μm	illite, chl.	0.60	0.42	Diagenesis									
Dob-389.6 2-1μm	illite, kaol., chl.	0.42		Upper anchizone	95		5	1000±12		1081.8 ± 25.0	5.97	99.7	153.5
Dob-389.6 <2μm	illite, kaol., chl.	0.43		Upper anchizone	90		10	1033 ± 25		1071.2 ± 25.0	6.53	99.7	165.7
Dob-389.6 1-0.5μm	illite, kaol., chl.	0.51		Lower anchizone	90		10			1037.8 ± 24.0	7.32	99.6	178.1
Dob-389.6 0.5-0.1μm	illite, kaol.	0.62		Diagenesis	80		20	1000±12		1053.0 ± 24.3	7.20	99.7	178.6
Dob-389.6 <0.5μm	illite, kaol.	0.63		Diagenesis						981.8 ± 22.6	7.63	99.8	172.7
Dob-389.6 <0.1μm	illite, kaol.	1.00		Diagenesis						905.4 ± 20.9	6.62	99.6	135.0
Dob-417 <2μm	illite, kaol., chl.	0.50		Lower anchizone									
Dob-441 >2μm	illite, kaol., chl.	0.36		Upper anchizone						1312.3 ± 30.7	3.72	99.5	124.5
Dob-441 <2μm	illite, kaol., chl.	0.42		Upper anchizone	95		5	1033 ± 25	1068.1 ± 1.8	1148.7 ± 26.9	4.98	99.3	138.7

1225

Dob-441 <1µm	illite, kaol., chl.	0.51		Lower anchizone	95	5			1086.5 ± 25.1	6.10	99.4	157.7
Dob-441 <0.5µm	illite, kaol., chl.	0.42		Upper anchizone					1063.3 ± 24.4	6.05		
Dob-449.1 <2µm	illite, kaol., chl.	0.29		Epizone	100		1033 ± 25		949.1 ± 22.2	6.40	99.5	138.6
Dob-449.1 2-0.5µm	illite, kaol., chl.	0.39		Upper anchizone			1000±12		924.9 ± 21.4	6.63	99.8	138.9
Dob-449.1 1-0.5µm	illite, kaol., chl.	0.35		Upper anchizone					903.1 ± 20.9	6.73	99.6	136.8
Dob-449.1 <0.5µm	illite, kaol., chl.	0.37		Upper anchizone					912.6 ± 21.1	5.43	100	111.9
Dob-449.3 >2µm	kaol., illite, chl.	0.14		Epizone					1259.0 ± 29.1	0.402	100	12.70
Dob-449.3 <2µm	illite, kaol., chl.	0.19		Epizone								
Dob-449.3 2-1µm	kaol., chl., illite	0.21		Epizone					1047.7 ± 24.2	0.294	100	7.24
Dob-449.3 1-0.5µm	kaol., chl., illite	0.27		Epizone					1117.2 ± 25.8	0.554	99.4	14.87
Dob-449.3 0.5-0.2µm	kaol., chl., illite	0.25		Epizone					950.9 ± 22.0	6.02	99.7	130.7
Dob-449.3 <0.5µm	kaol., chl., illite	0.25		Epizone					1004.4 ± 23.2	0.428	99.8	9.98
Dob-476.6 >2µm	illite, kaol., chl.	0.26		Epizone					1170.4 ± 27.4	2.15	99.5	61.43
Dob-476.6 2-1µm	illite, kaol., chl.	0.29		Epizone	100				975.7 ± 22.2	4.43	99.4	101.7
Dob-476.6 <2µm	illite, kaol., chl.	0.33		Upper anchizone	100		1000 ± 12	994.6 ± 2.2	983.7 ± 23.0	4.80	99.4	108.9
Dob-476.6 <1µm	illite, kaol., chl.	0.31		Epizone	100				922.2 ± 21.2	6.18	100.0	129.0
Host whole rock												
JC-360.6 <2µm	illite	0.48		Lower anchizone								
JC-360.6 2-1µm	illite	0.68		Diagenetic					1066.9 ± 24.6	6.13	99.61	157.7
JC-360.6 1-0.5µm	illite	0.82		Diagenetic					1065.4 ± 24.6	6.90	99.7	173.8
JC-360.6 0.5-0.2µm	illite	0.52		Lower anchizone					1053.8 ± 24.3	6.68	99.2	165.8
JC-360.6 <0.2µm	illite	0.78		Diagenesis					928.3 ± 47.6	6.63	99.05	139.6
JC-490.2 <2µm	illite, chl.	0.46	0.36	Lower anchizone								
JC-500 <2µm	illite, chl.	0.51	0.36	Lower anchizone								
JC-500 2-1µm	illite, chl.	0.66		Diagenesis					1092.0 ± 25.2	3.37	99.69	87.71
JC-500 1-0.5µm	illite, chl.	0.62		Diagenesis					1076.8 ± 24.8	5.15	99.67	131.6
JC-500 0.5-0.2µm	illite, chl.	0.64		Diagenesis					1066.7 ± 24.5	5.39	99.47	135
JC-500 <0.2µm	illite, chl.	0.63		Diagenesis					878.3 ± 45.1	5.41	99.02	106.2
Dob-499.4 >2µm	illite, kaol., chl.	0.22		Epizone					1156.2 ± 26.6	0.37	97.1	10.26
Dob-499.4 <2µm	illite, kaol., chl.	0.20		Epizone								
Dob-499.4 2-1µm	illite, kaol., chl.	0.23		Epizone					1115.8 ± 25.7	2.03	99.6	54.38
Dob-499.4 1-0.5µm	illite, kaol., chl.	0.20		Epizone					1047.3 ± 24.1	5.08	99.5	125.1
Dob-499.4 0.5-0.2µm	illite, kaol., chl.	0.18		Epizone					1068.2 ± 24.6	3.30	99.3	83.41
Dob-499.4 <0.2µm	illite, kaol., chl.	0.21		Epizone					1025.6 ± 52.6	3.63	97.5	86.97

Calibration of the illite crystallinity (IC) and chlorite crystallinity (ChC) values and determination of very-lowe-grade- metamorthic zones. has been done according to Warr and Mählmann (2015) and Warr and Cox (2016). kaol. = kaolinite, chl. = chlorite. Illite polytype percentages are relative to total illite

1226

1227

Table 2. K-Ar standard and airshot data.

STANDARD ID	K [%]	Rad. ^{40}Ar (mol/g)	Rad. ^{40}Ar (%)	Age (Ma)	Error (Ma)	% difference from recommended reference age
HD-B1-137	7.96	3.3431E-10	89.76	24.1	0.4	-0.01
LP6-151	8.37	1.9477E-09	97.28	129.4	1.8	1.19
HD-B1-139	7.96	3.4214E-10	92.33	24.6	0.3	1.73
LP6-153	8.37	1.9465E-09	97.32	129.3	1.7	1.12
HD-B1-140	7.96	3.3805E-10	92.39	24.3	0.3	0.50
LP6-154	8.37	1.9196E-09	97.39	127.6	1.6	-0.23
HD-B1-141	7.96	3.4399E-10	92.86	24.8	0.3	2.27
LP6-155	8.37	1.9304E-09	97.69	128.3	1.6	0.31
HD-B1-142	7.96	3.4500E-10	93.28	24.8	0.3	2.56
LP6-156	8.37	1.9285E-09	97.59	128.2	1.7	0.21
HD-B1-147	7.96	3.4124E-10	92.88	24.6	0.3	1.45
LP6-161	8.37	1.9257E-09	97.13	128.0	1.7	0.07
HD-B1-148	7.96	3.3633E-10	90.67	24.2	0.3	0.00
LP6-162	8.37	1.9236E-09	97.21	127.9	1.7	-0.03
HD-B1-149	7.96	3.3562E-10	90.93	24.2	0.3	-0.21
LP6-163	8.37	1.9234E-09	97.21	127.9	1.6	-0.04

Airshot ID	^{40}Ar/^{36}Ar	+/-
AS131-AirS-1	295.67	0.45
AS131-AirS-2	293.43	0.46
AS133-AirS-1	298.42	0.14
AS133-AirS-2	297.35	0.29
AS134-AirS-1	295.81	0.14
AS134-AirS-2	296.65	0.08
AS135-AirS-1	296.59	0.13
AS135-AirS-2	296.76	0.17
AS136-AirS-1	295.22	0.24
AS136-AirS-2	296.69	0.27
AS141-AirS-1	295.85	0.28
AS141-AirS-2	296.53	0.23
AS142-AirS-1	294.87	0.23
AS142-AirS-2	296.52	0.18
AS143-AirS-1	294.16	0.20
AS143-AirS-2	296.81	0.17

HD-B1: Hess and Lippolt (1994).

LP-6: Odin et al. (1982).

Recommended ^{40}Ar/^{36}Ar value: 295.5: Steiger and. Jäger (1977).

1228 The accepted age value of HD-B1 is 24.21 ± 0.32 Ma and 127.9 ± 1.5 Ma for LP6

Table 3. ^{87}Rb-^{86}Sr data for the untreated (U) and acid leached residues (R) of different clay fractions from the Milungera Basin fault gouges.

Sample	Size farction (μm)	Rb (ppm)	Sr (ppm)	$^{87}Rb/^{86}Sr$	$^{87}Sr/^{86}Sr$	±2σ
JC-343.3U	<2	263.8	244.7	3.14	0.771035	0.000008
JC-360.7U[b-c]	<2	270.5	303.9	2.59	0.757396	0.000009
JC-360.7R[b-c]	<2	253.7	269.0	2.74	0.759576	0.000009
JC-360.7R	2-1	279	361.1	2.25	0.754344	0.000008
JC-360.7L	2-1	61.96	914.2	0.196	0.715331	0.000006
JC-360.7R[d]	<0.5	288.7	222.1	3.79	0.778401	0.000005
JC-360.7L	<0.5	68.94	906.2	0.220	0.715632	0.000006
JC-387.8U[b]	<2	203.7	564.6	1.05	0.734125	0.000009
JC-387.8R[b-c]	<2	201.6	537.4	1.09	0.735621	0.000007
JC-408U	<2	273.0	259.4	3.06	0.768788	0.000009
JC-440.5U[b]	<2	206.8	637.0	0.941	0.733108	0.000007
JC-440.5R[b-c]	<2	213.2	627.4	0.986	0.734396	0.000009
JC-440.5R	<0.5	279.2	240.1	3.38	0.765505	0.000006
JC-440.5L	<0.5	26.75	378.4	0.205	0.716576	0.000006
Dob-389.6U[d]	2	239.5	184.5	3.78	0.778229	0.000009
Dob-389.6R[e]	2-1	255.0	254.5	2.92	0.769394	0.000006
Dob-389.6R[e]	<0.5	268.6	201.0	3.89	0.783259	0.000008
Dob-389.6L	<0.5	22.08	612.8	0.10	0.712000	0.000006
Dob-441U[d]	<2	134.8	121.6	3.23	0.770115	0.000008
Dob-441R	2-1	200.7	203.4	2.87	0.767702	0.000006
Dob-441R	<1	202.1	201.8	2.91	0.768636	0.000007
Dob-441L	<1	20.5	399.5	0.149	0.720827	0.000006
Dob-449.1U[d]	<2	214.7	337.0	1.85	0.750186	0.000009
Dob-449.1R[d]	<2	218.9	326.1	1.95	0.751971	0.000014
Dob-449.1R[d]	2-1	242.0	378.8	1.86	0.749952	0.000006
Dob-449.1L	2-1	13.59	265.7	0.148	0.718102	0.000006
Dob-476.6U[e]	<2	190.0	521.6	1.06	0.744176	0.000009
Dob-476.6R[e]	<2	200.2	517.7	1.12	0.744209	0.000007

U= untreated, R = residue, L = leachate

Samples with superscript b, c, d, and e are used in Fig. 8b, c, d, and e, respectively.

Table 4. Trace element data (ppm) for the fault gouge illites.

Sample	JC-360.7	JC-387.8	JC-440.5	Dob-389.6	Dob-449.1	Dob-476.6	PAAS
La	89.8	281.5	242.3		328.0	396.2	38.0
Ce	193.9	619.1	519.4		591.8	773.3	80.0
Pr	19.9	63.1	54.3		73.1	80.2	8.90
Nd	69.1	225.6	187.3		257.0	271.5	32.0
Sm	12.8	39.1	32.2		44.5	46.3	5.60
Eu	2.22	4.32	4.22		7.30	7.01	1.10
Gd	9.27	24.3	21.2		29.8	28.7	4.70
Tb	1.05	2.07	2.59		3.70	3.23	0.77
Dy	5.09	7.22	12.9		20.2	15.9	4.40
Ho	0.94	1.17	2.42		4.36	3.29	1.00
Er	2.59	3.27	6.66		14.2	10.5	2.90
Tm	0.37	0.43	0.97		2.47	1.74	0.40
Yb	2.36	2.81	6.29		18.0	12.3	2.80
Lu	0.35	0.41	0.93		2.87	1.93	0.43
Th	80.8	110.9	83.6		107.7	149.1	14.60
U	7.54	8.43	18.6		32.2	40.3	3.10
Sc	20.7	10.2	11.2		91.4	58.1	16.00
$(La/Lu)_c$	29	23	76		13	29	10
Th/Sc	3.9	10.9	7.5		1.2	2.6	0.9
Th/U	10.7	13.2	4.5		3.3	3.7	4.7

1231

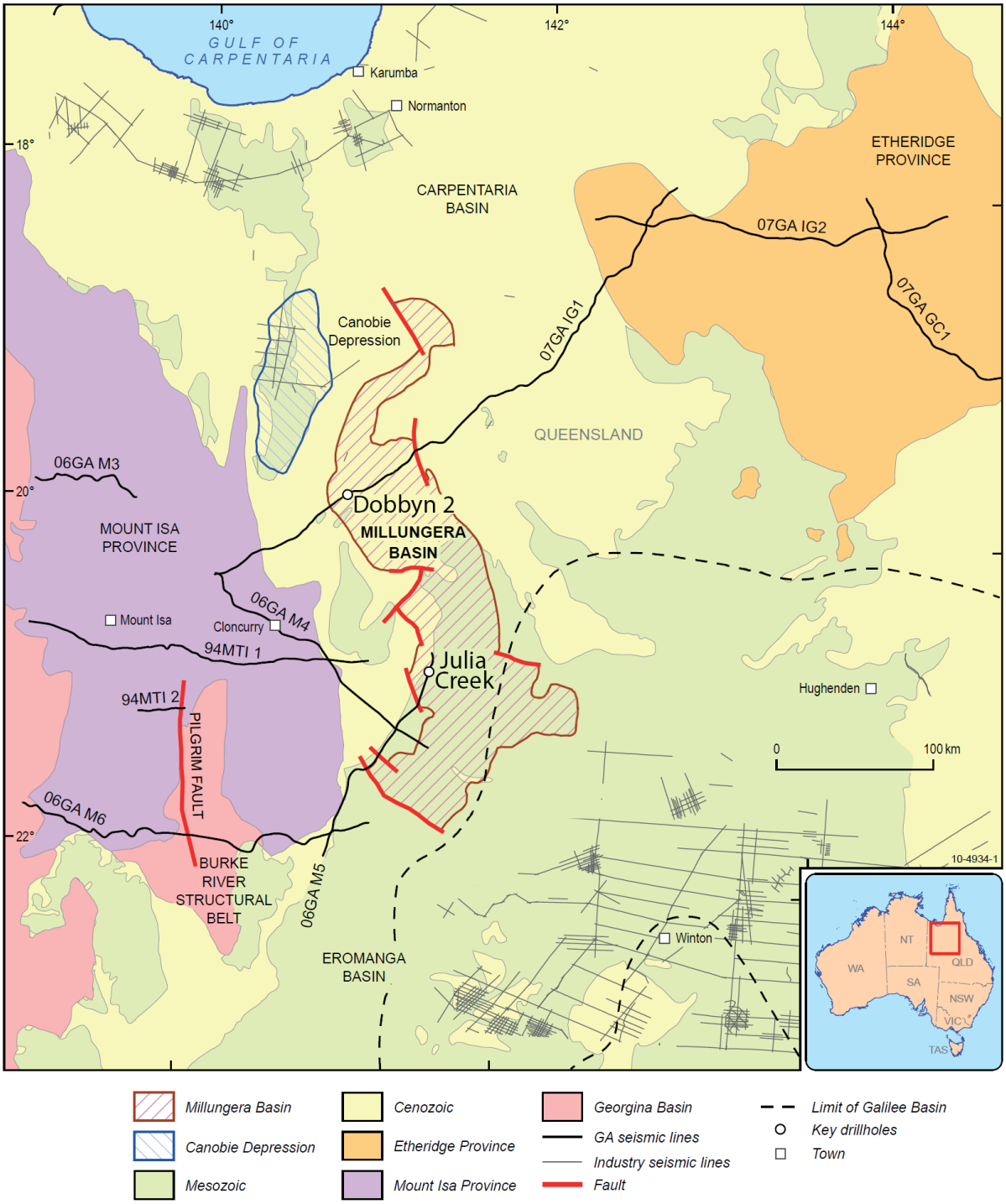
GULF OF CARPENTARIA
140°
142°
144°
18°
20°
22°
Karumba
Normanton
CARPENTARIA BASIN
ETHERIDGE PROVINCE
07GA IG2
07GA GC1
07GA IG1
Canobie Depression
QUEENSLAND
06GA M3
Dobbyn 2
MILLUNGERA BASIN
MOUNT ISA PROVINCE
Mount Isa
Cloncurry
06GA M4
94MTI 1
Julia Creek
94MTI 2
PILGRIM FAULT
Hughenden
0
100 km
06GA M6
BURKE RIVER STRUCTURAL BELT
06GA M5
EROMANGA BASIN
Winton
10-4934-1
NT
QLD
WA
SA
NSW
VIC
TAS
Millungera Basin
Canobie Depression
Mesozoic
Cenozoic
Etheridge Province
Mount Isa Province
Georgina Basin
GA seismic lines
Industry seismic lines
Fault
Limit of Galilee Basin
Key drillholes
Town

Figure 1a

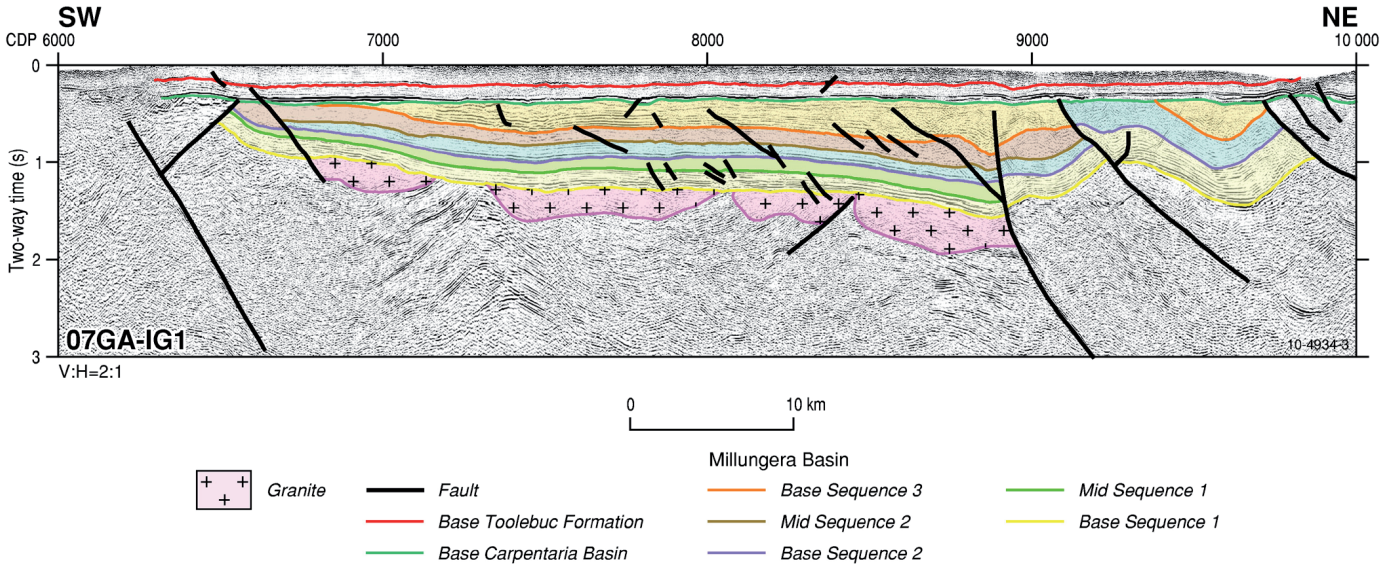

1255

1256 Figure 1b

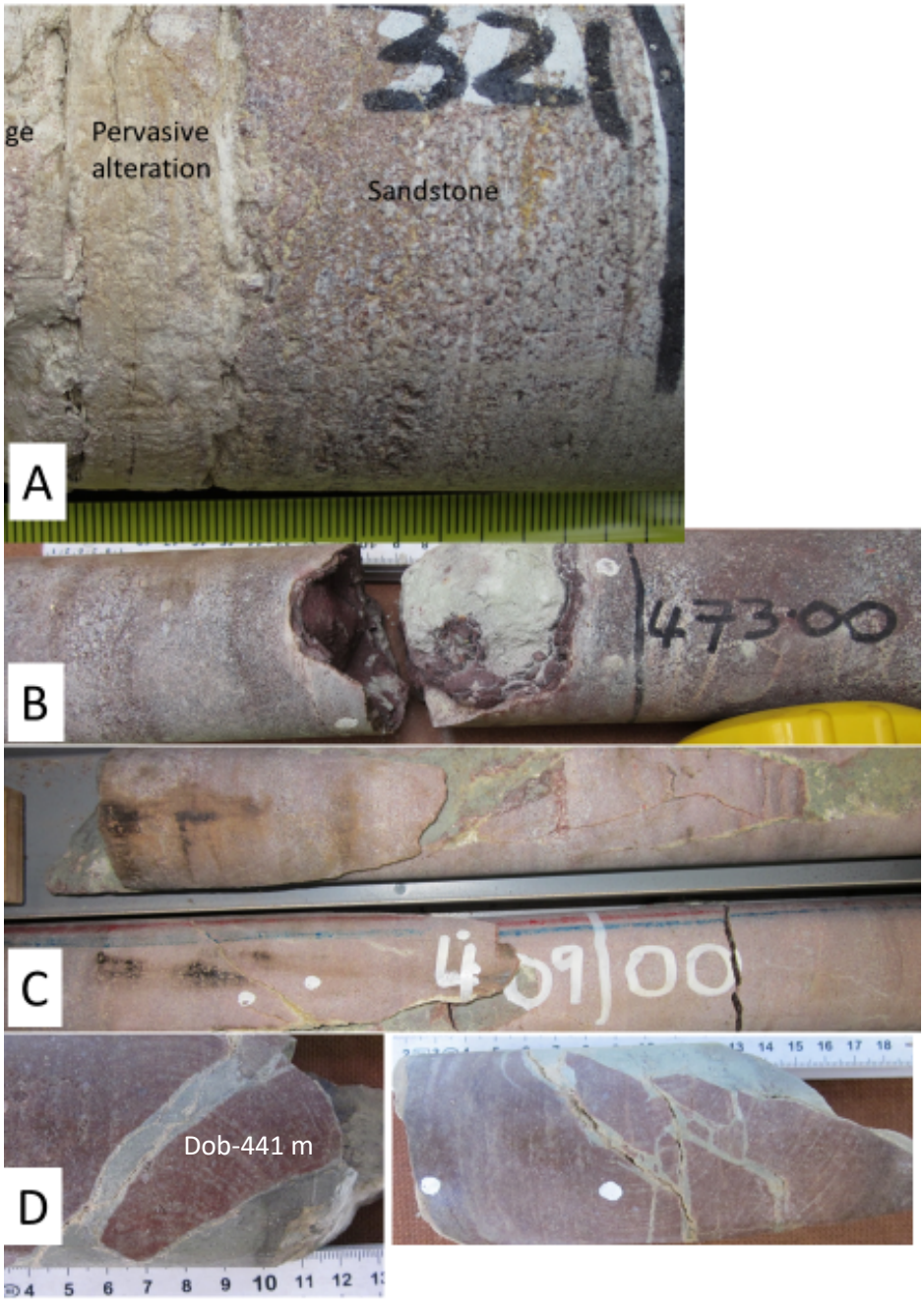

1257

Fig. 2

1258

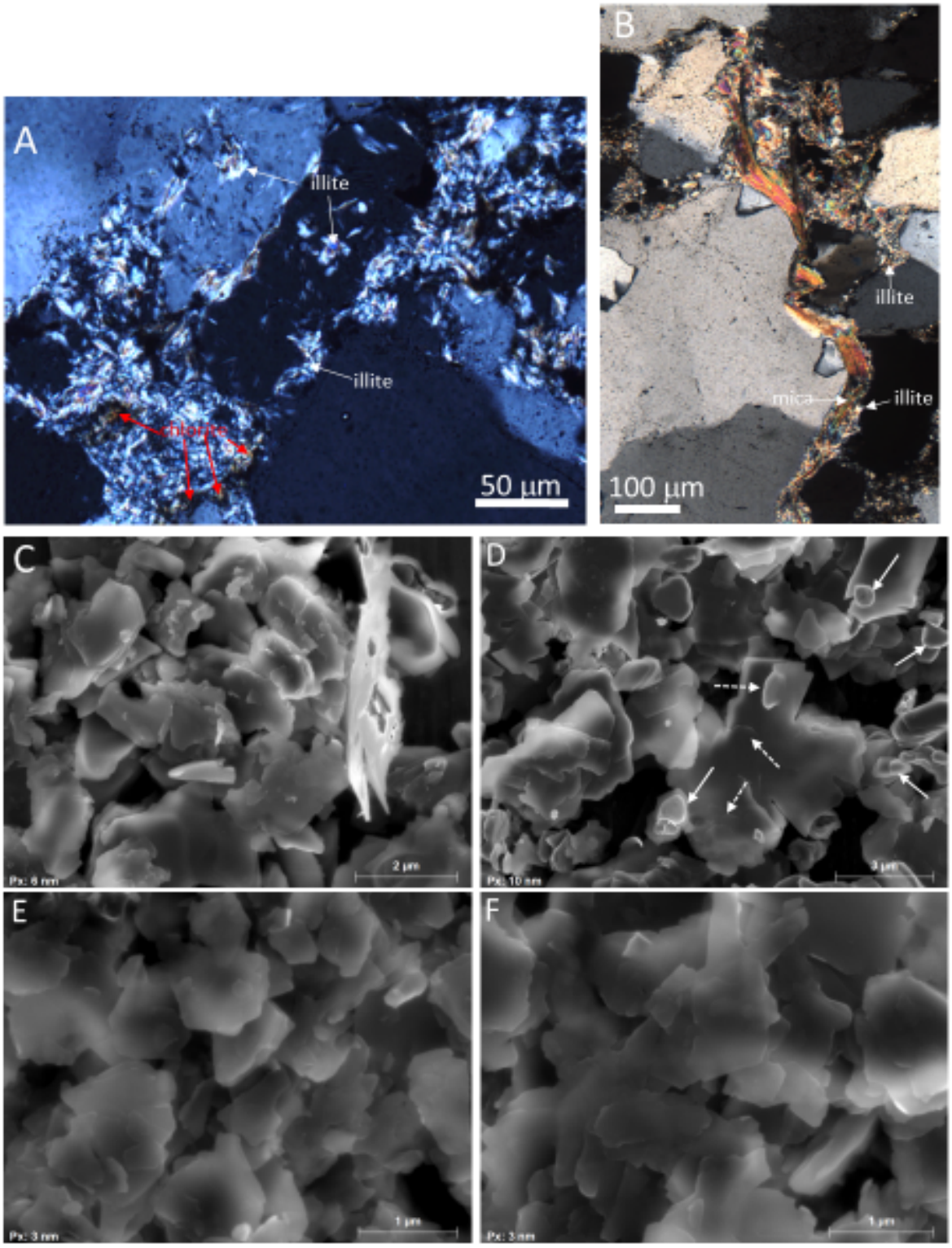

Figure 3.

1259

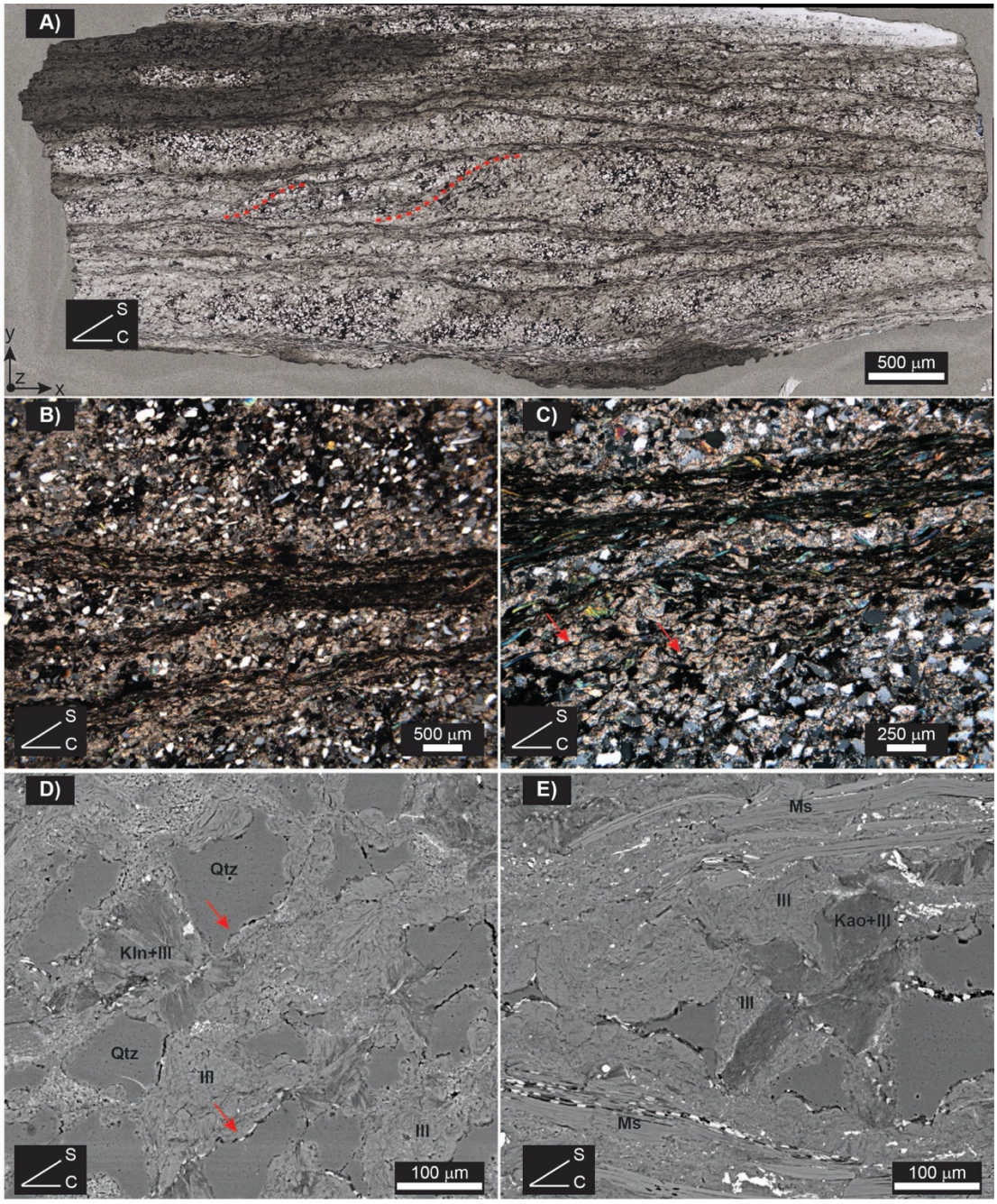
A)
S
C
y
z
x
500 µm
B)
S
C
500 µm
C)
S
C
250 µm
D)
Qtz
Kln+Ill
Qtz
Ill
Ill
S
C
100 µm
E)
Ms
Ill
Kao+Ill
Ill
Ms
S
C
100 µm

Figure 4

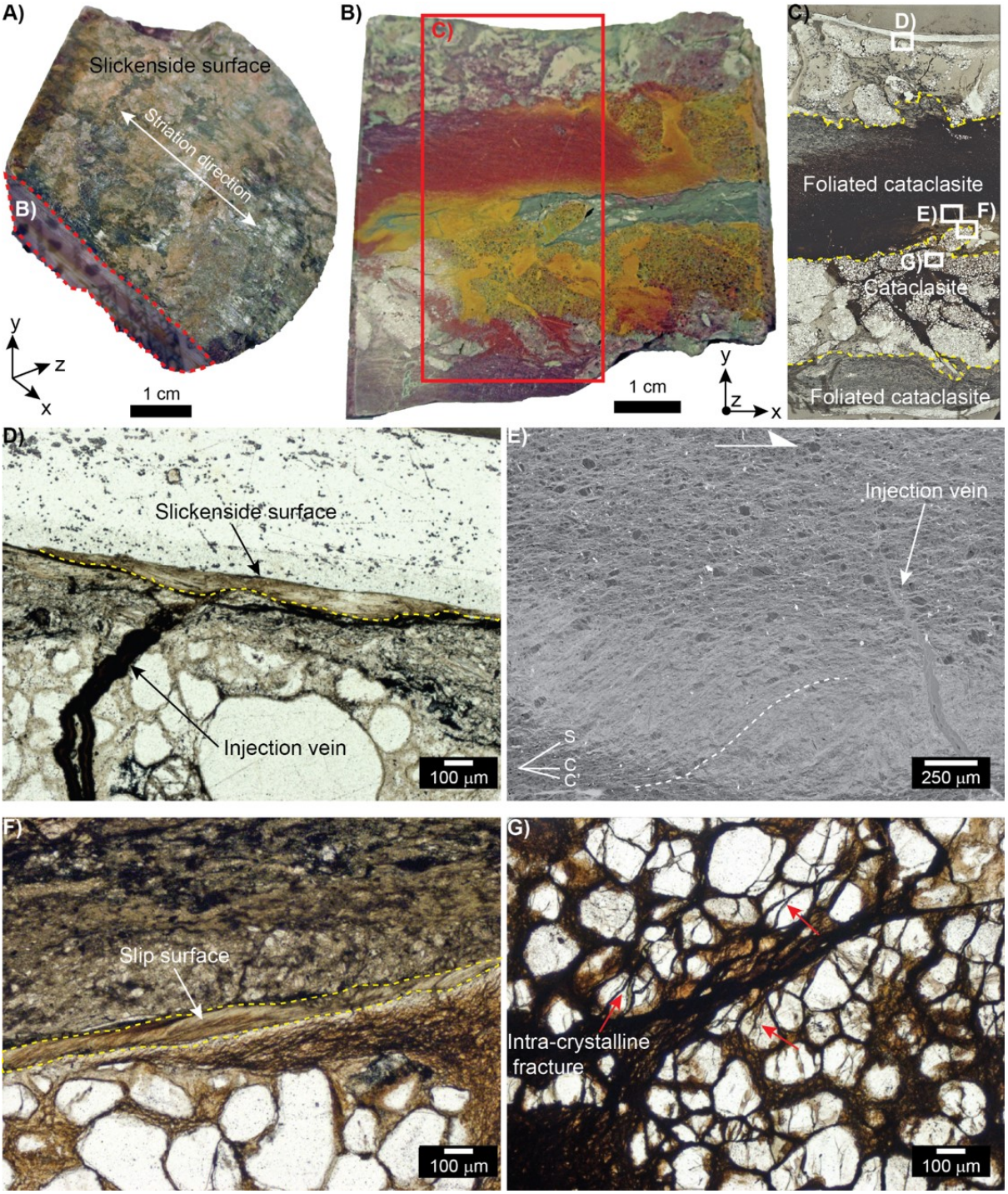
A)
Slickenside surface
Striation direction
B)
y
z
x
1 cm
B)
C)
1 cm
y
z
x
C)
D)
Foliated cataclasite
E)
F)
G)
Cataclasite
Foliated cataclasite
D)
Slickenside surface
Injection vein
100 µm
E)
Injection vein
S
C
C'
250 µm
F)
Slip surface
100 µm
G)
Intra-crystalline
fracture
100 µm

Figure 5

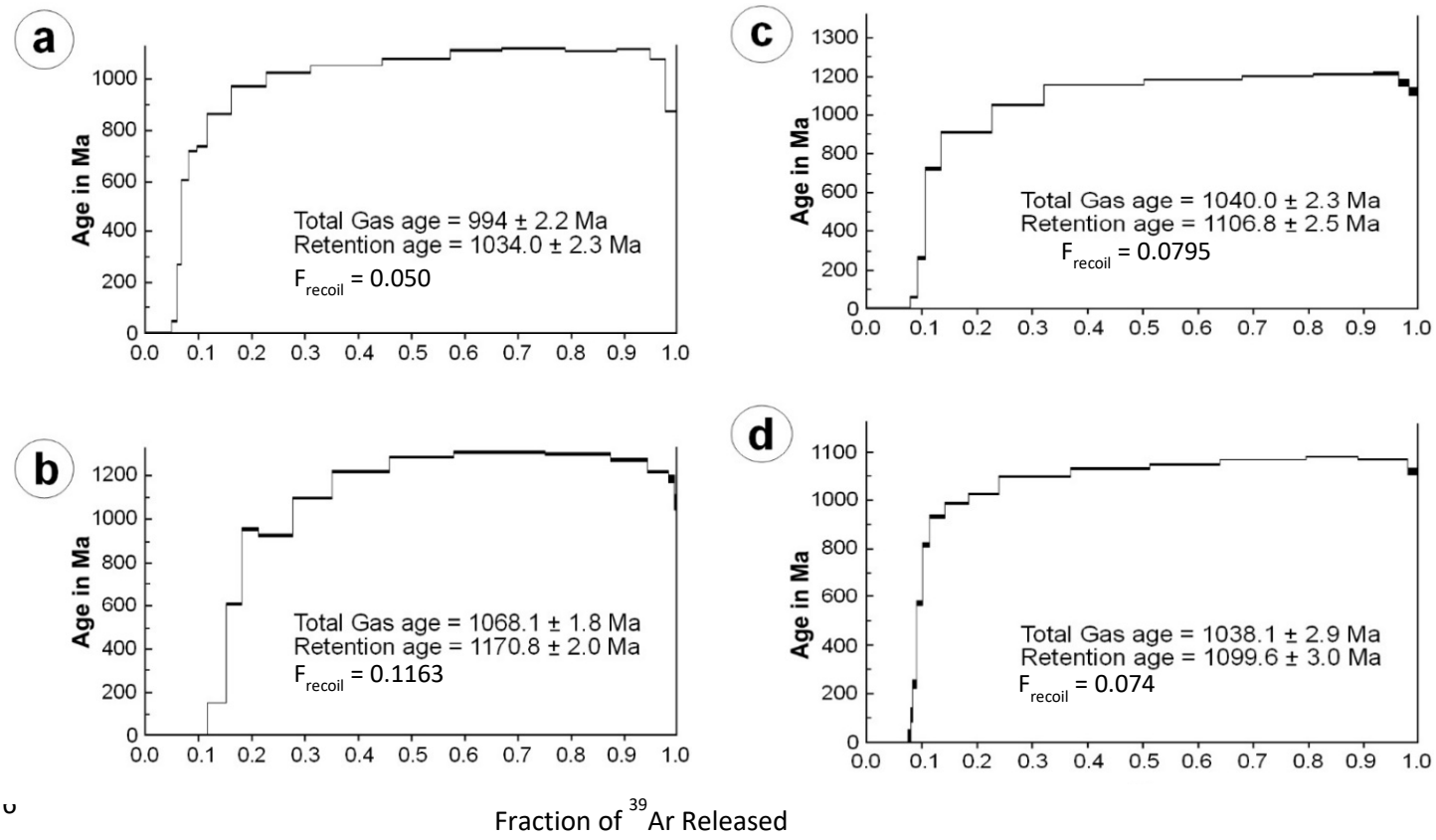
a
Age in Ma
Total Gas age = 994 ± 2.2 Ma
Retention age = 1034.0 ± 2.3 Ma
F recoil = 0.050
c
Age in Ma
Total Gas age = 1040.0 ± 2.3 Ma
Retention age = 1106.8 ± 2.5 Ma
F recoil = 0.0795
b
Age in Ma
Total Gas age = 1068.1 ± 1.8 Ma
Retention age = 1170.8 ± 2.0 Ma
F recoil = 0.1163
d
Age in Ma
Total Gas age = 1038.1 ± 2.9 Ma
Retention age = 1099.6 ± 3.0 Ma
F recoil = 0.074
Fraction of 39Ar Released

Figure 6

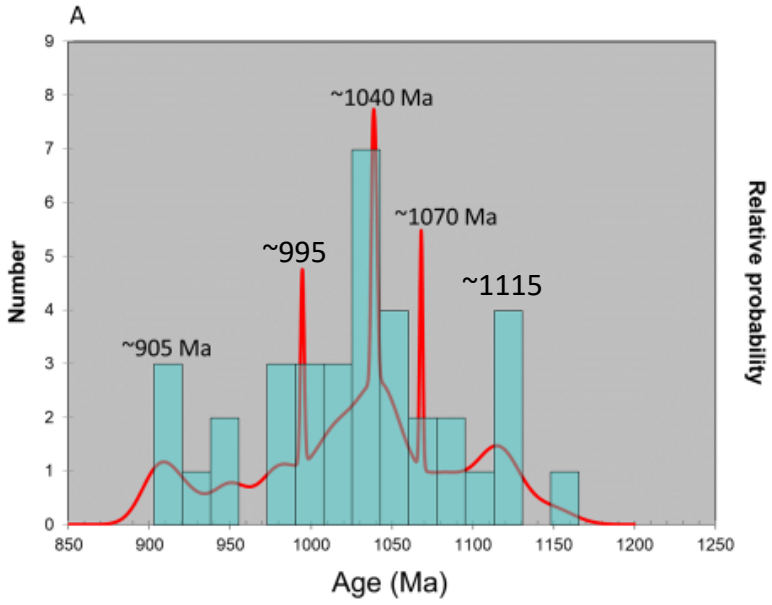

Figure 7a

1278

1279

1280 B

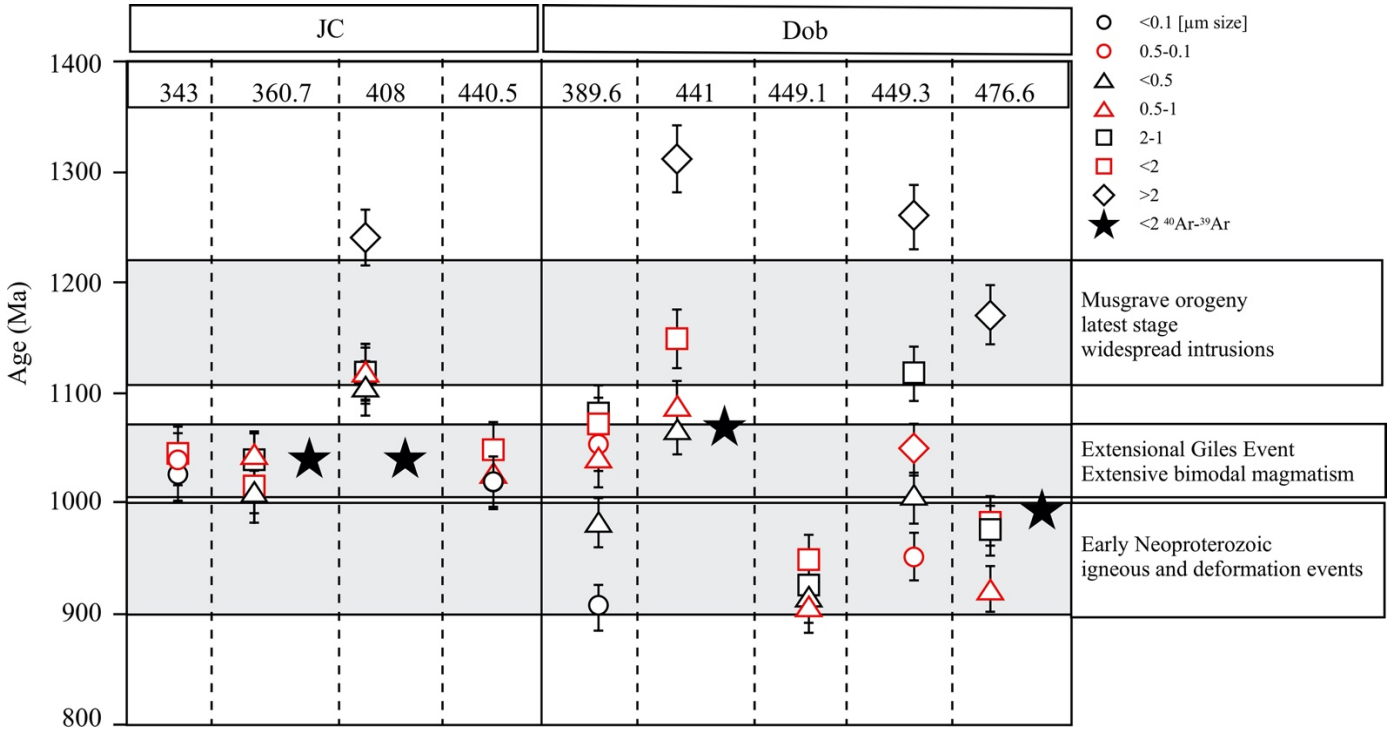

1281

1282 Fig. 7b

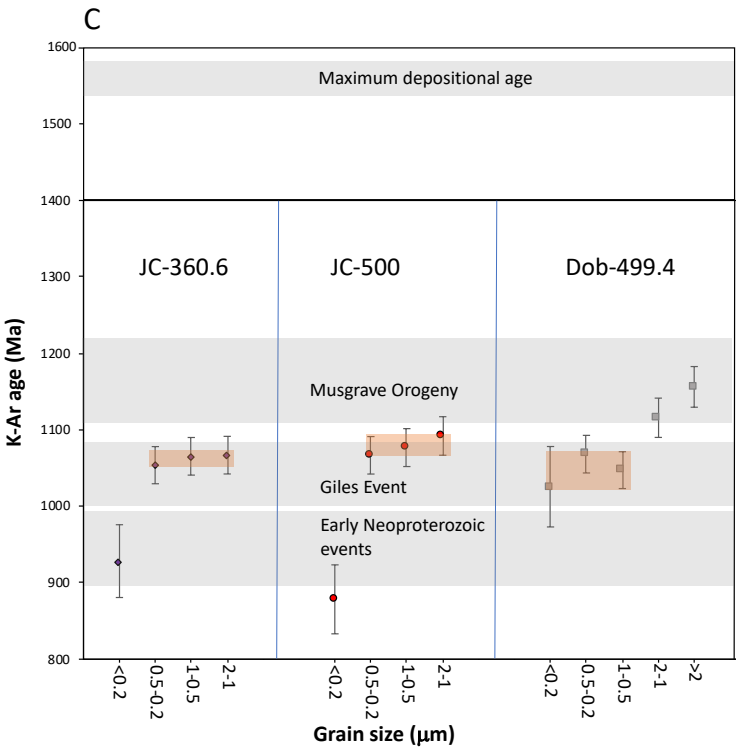

Figure 7c

1283

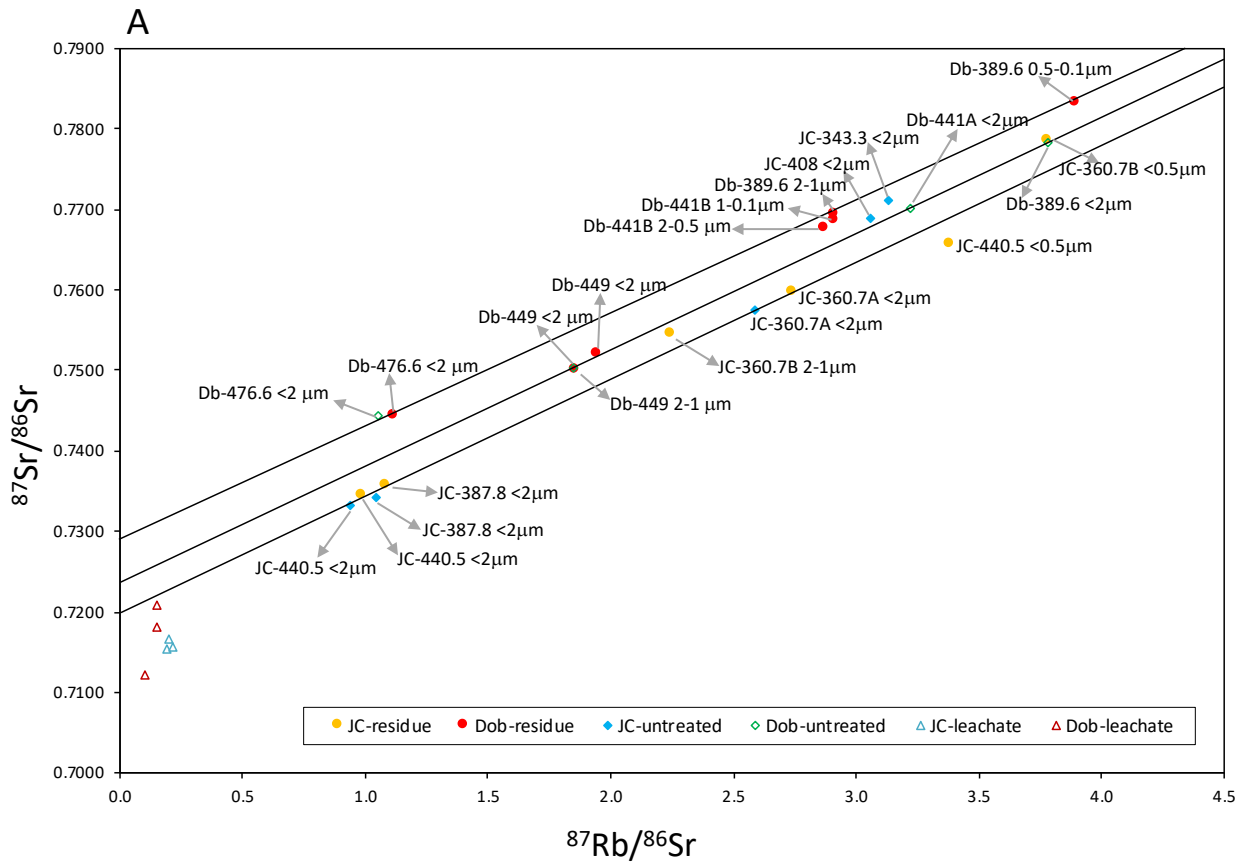

Figure 8a

1284

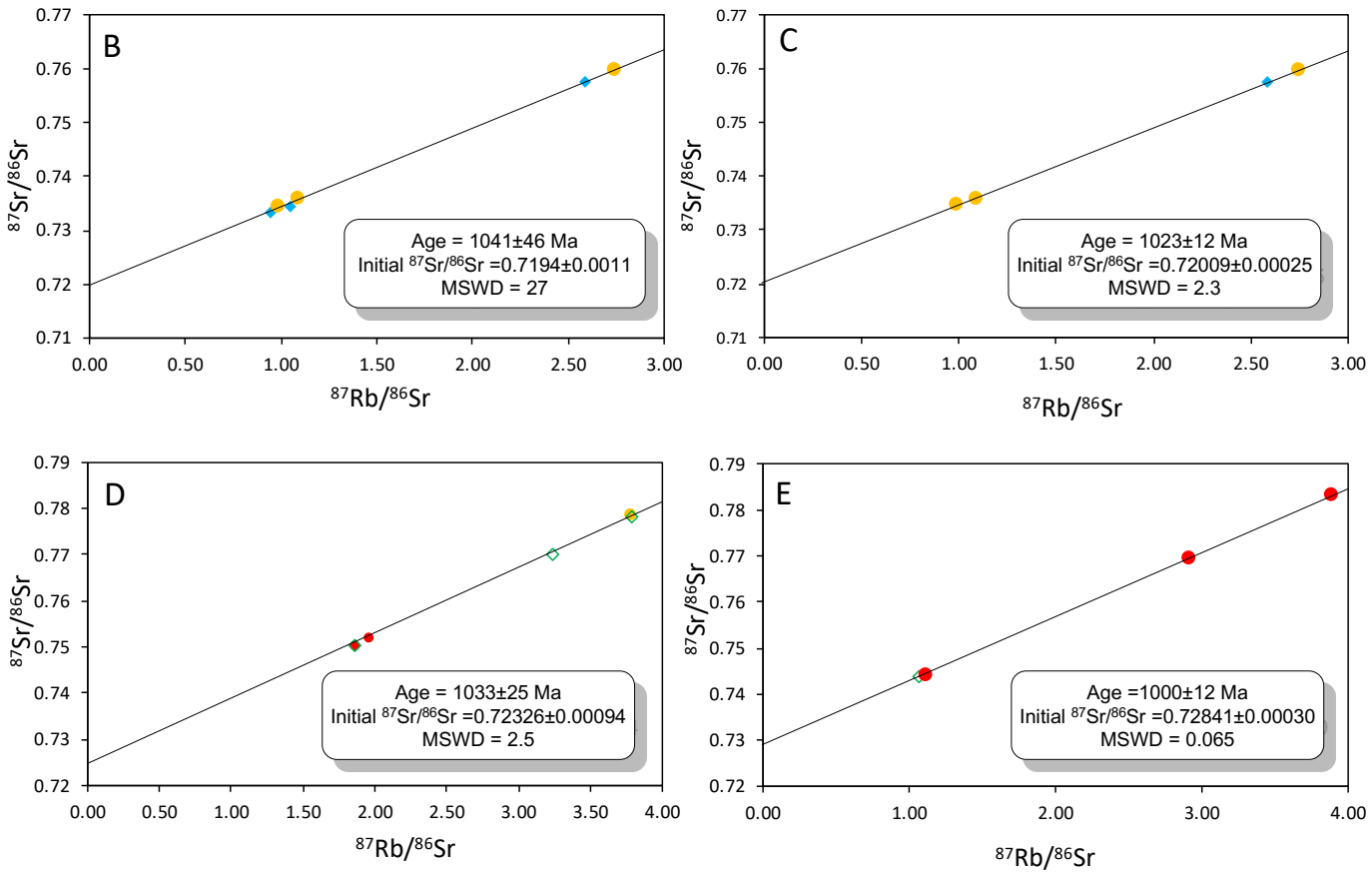

Figure 8b-e

1285

1286

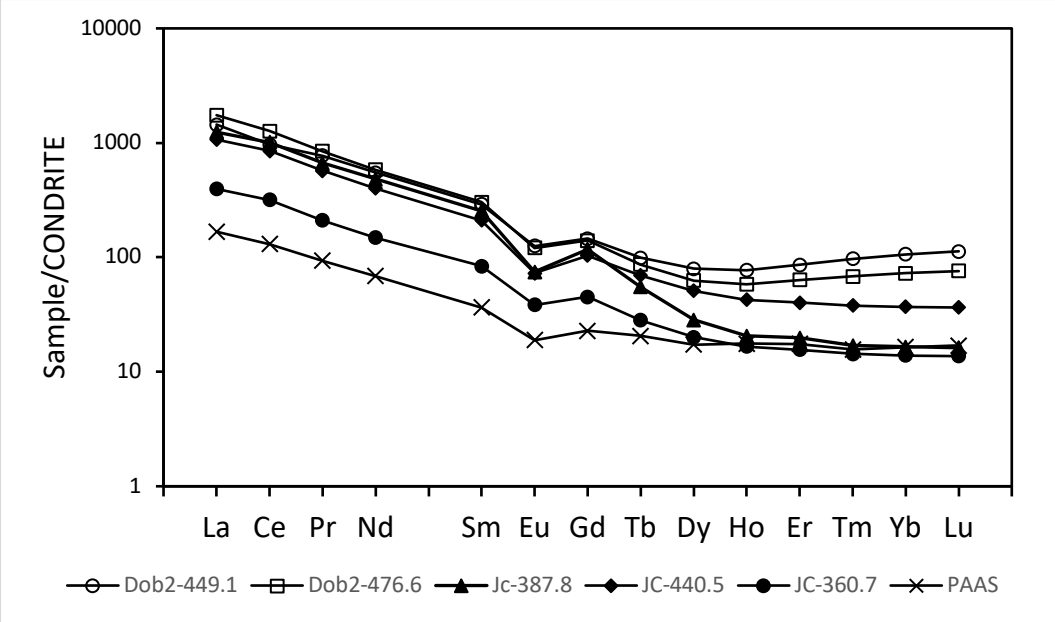

1287

1288 Figure 9

1289

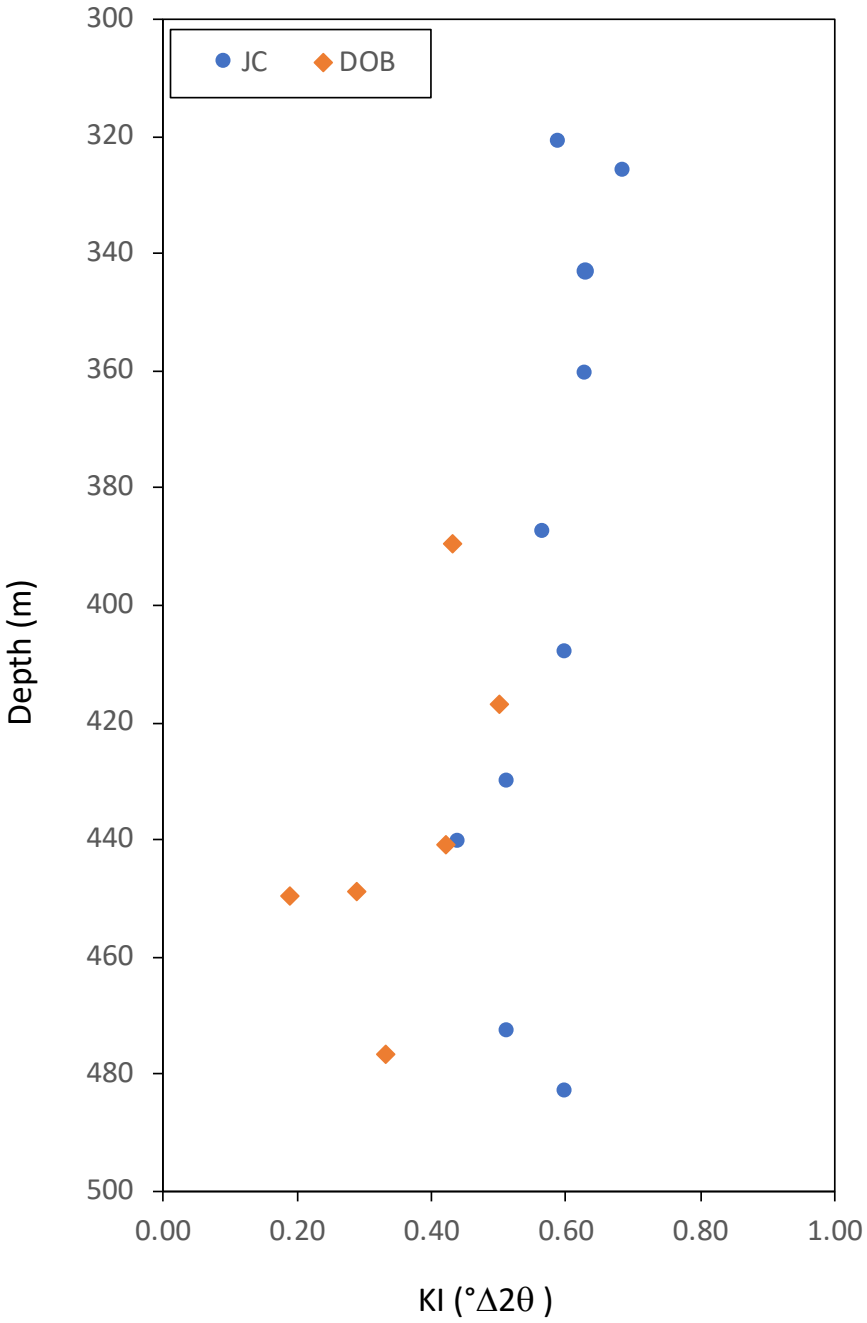

1290

1291 Figure 10

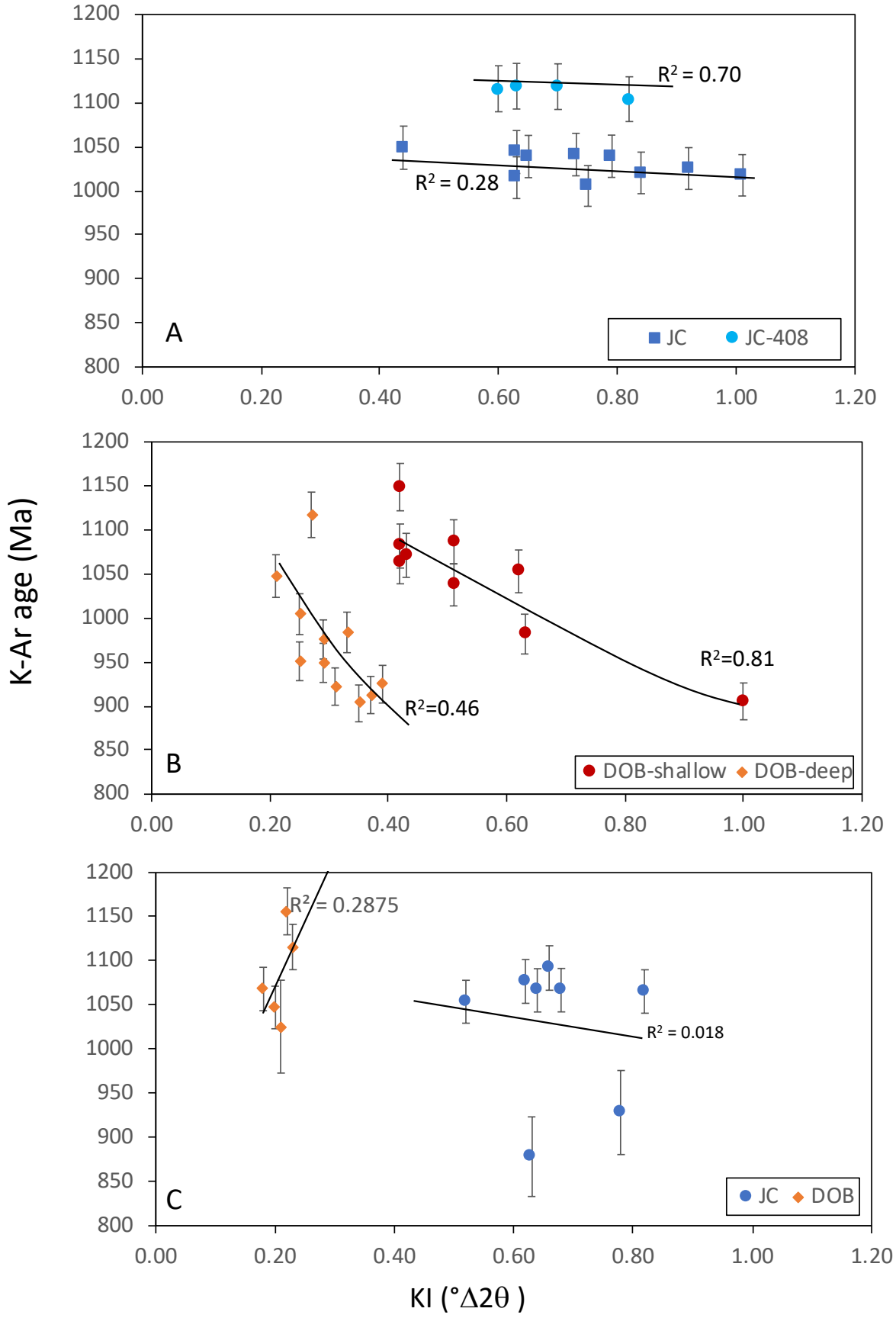
K-Ar age (Ma)
KI (°Δ2θ)
A
R² = 0.70
R² = 0.28
JC
JC-408
B
R²=0.81
R²=0.46
DOB-shallow
DOB-deep
C
R² = 0.2875
R² = 0.018
JC
DOB

Figure 11

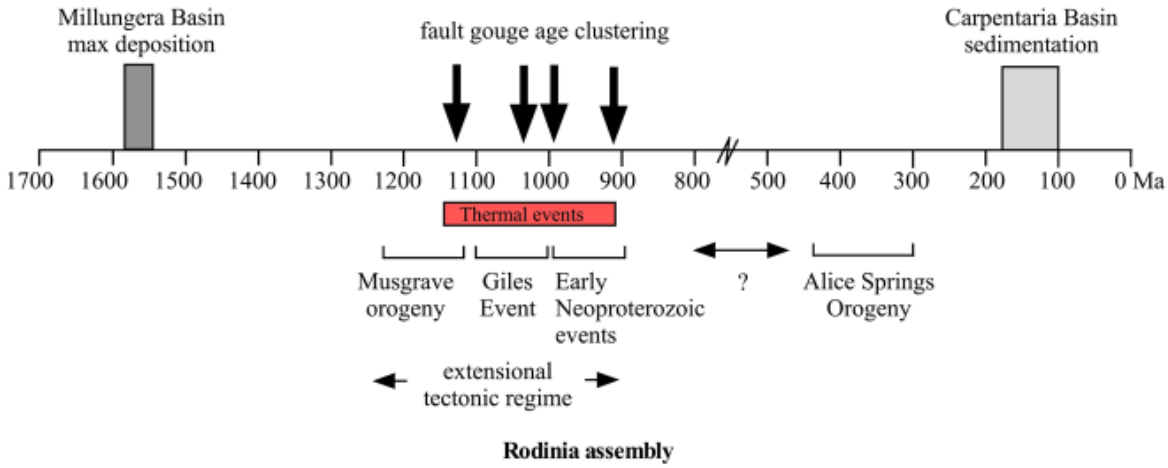

1294

1295 Figure 12

1296